Fuel 399 (2025) 135626

Contents lists available at ScienceDirect

Fuel

journal homepage: www.elsevier.com/locate/fuel

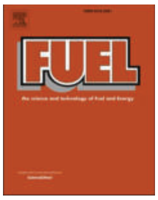

Full Length Article

Experimental and numerical characterization of a single-hole LPDI Hydrogen injector: identification of a suitable inert replacement for Hydrogen jet studies

Sebastiano Breda [a,*], Mauro Magnani [a], Manuel Martino [b], Stefano Fontanesi [a], Lucio Postrioti [b]

[a] *Università degli Studi di Modena e Reggio Emilia, Dipartimento di Ingegneria "Enzo Ferrari", Via Pietro Vivarelli 10, 41125 Modena, Italy*
[b] *Università degli Studi di Perugia, Dipartimento di Ingegneria, Via Goffredo Duranti 93, 06125 Perugia, Italy*

ARTICLE INFO

Keywords:
Hydrogen injector
Gas injection
CFD-3D
Experimental
Under expanded gas jets
Inert gases

ABSTRACT

In recent years, climate change has exerted great pressure for the development of both existing and new technologies to reduce green-house gases emissions. The transportation sector has been, and is still, heavily impacted by this green revolution, which is driving the automotive world towards electrification, at least for light- and mid-duty vehicles. In parallel, the development of Hydrogen powertrains, both as Internal Combustion Engines (ICEs) and Fuel Cells (FCs) has found new impulse, being it a solution to help the transportation sector, for heavy- as well for light-duty applications, to reach carbon neutrality. Conversion of conventional thermal engines into carbon free fuelled ones could speed up the achievement of the goals set by COP21 for the 2030–2050 agenda. The result would be environmentally effective and cost sustainable, avoiding obsolescence for the internal combustion engine technology. For the fossil-to-Hydrogen conversion, a key role is played by the injection system, which is responsible for both the fuel mass delivery rate and the fuel jet morphology in the combustion chamber, thus highly impacting air–fuel mixing, heat release rate and pollutant formation. For these reasons, a detailed understanding of the Hydrogen injector is mandatory to achieve an efficient and "clean" engine operation. In this work, a detailed numerical and experimental characterization of a single-hole gas injector is presented using Argon (Ar), Helium (He), and Nitrogen (N_2) as substitutes for Hydrogen (H_2). The use of inert gases is a common practice in the literature to reduce experimental costs and enhance safety. However, the influence of gas properties on measured quantities is not yet fully understood. The experimental data are used to develop and validate a CFD methodology to simulate gas jets and to numerically extrapolate the injector's behaviour when using Hydrogen. This combined experimental–numerical approach enables definitive conclusions regarding the substitution of H_2 with inert gases. Strong similarities between He and H_2 confirm helium as the most suitable surrogate gas to characterize jet cone angle and penetration while near nozzle flow details are well reproduced by using a bi-atomic gas such as N_2.

1. Introduction

The increasingly stringent emission policies of the recent years are revolutionising the transportation sector, bringing internal combustion engine technology to a major crossroad. The agreements achieved during the Paris conference (COP21) [1] have set a maximum limit of global temperature increment at 2 °C. To reach that objective, UE has imposed, through a regulation of the European Parliament [2], a ban on the sale of gasoline and diesel fuelled cars from 2035 [3] and in general of the internal combustion engines technology operated with carbon-

---

Abbreviations: AMR, Automatic Mesh Refinement; COP21, The 21st Conference of the Parties; BEVs, Battery Electric Vehicles; CC, Combustion Chamber; CF, Coupled Flow; CFD, Computational Fluid Dynamics; CNG, Compressed Natural Gas; EMI, Einspritz Mengen Indikator (Injection Quantity Indicator); ET, Energizing time; FCVs, Fuel Cell Vehicles; FSC, Fast Shutter Camera; HPDI, High Pressure Direct Injection; HSV, High Speed Video; ICEs, Internal Combustion Engines; LDV, Laser, Doppler Vibrometry; LPDI, Low Pressure Direct Injection; PFI, Port Fuel Injection; PID, Proportional Integral Derivative controller; RPM, Revolution per minutes; RANS, Reynolds-Averaged Navier-Stokes equations; SF, Segregated Flow.

[*] Corresponding author.

E-mail address: sebastiano.breda@unimore.it (S. Breda).

https://doi.org/10.1016/j.fuel.2025.135626
Received 8 October 2024; Received in revised form 28 April 2025; Accepted 7 May 2025

based fuels [4], a stark position to which manufacturers must comply as soon as possible, at least for passenger cars and light commercial vehicles. To reduce technical risks related to the exclusive use of only partially mature technologies such as BEVs and FCV, and to preserve the technological competitiveness of many European and Western countries, Hydrogen-fuelled thermal engines are increasingly seen as a potential contribution [5], given the maturity of the base technology and the moderately challenging development work required to adapt the ICE combustion systems and ancillary apparatuses to the use of carbon-free gaseous fuel. As a matter of fact, Hydrogen has long been seen as a promising alternative to fossil fuels due to the absence of CO_2 in the combustion products, attractive efficiency levels and marginal NO_x emissions, inherently resolving many of the on-board energy storage and recharging time issues of BEVs and the technology costs of FCV-based vehicles. Still, the actual climate impact of Hydrogen-fuelled engines strongly depends on the fuel production method. The greenest method to obtain Hydrogen is through water electrolysis from renewable energy sources; unfortunately, this method is affected by low efficiency and relatively high production costs [6,7]. Alternatively, Hydrogen can be produced through methane steam reforming process [8] with relatively low cost and high efficiency, but clearly with a non-zero CO_2 impact in a life-cycle perspective.

Despite the potential benefits offered by the use of a consolidated technology such as internal combustion engine, the conversion to Hydrogen fuelling is not immediate, due to the peculiar physical and chemical characteristics of the Hydrogen molecule [9]. Hydrogen combines very high laminar flame speed with large flammability range, thus enabling ultra-lean stable combustion, and therefore it opens the door for high engine thermal efficiency and low or negligible NO_x emissions. Nevertheless, Hydrogen is characterized by a low volumetric power density, together with a low liquefaction temperature. While the former, especially in conjunction with ultra-lean mixtures, results in a relevant penalty on brake specific power output, the latter increases the complexity of the on-board storage system for Hydrogen in gaseous phase [10]. To ensure a reasonable driving range avoiding the “range anxiety” typical of BEVs, a high-pressure Hydrogen on-board storage system is mandatory adopting technologies already developed for commercial FCVs [11,12], although at the cost of additional complexities such as material degradation [13] and safety issues [14]. Finally, the low ignition energy of Hydrogen makes combustion control difficult and increases the risk of surface ignition.

Similarly to many other liquid and gaseous fuels, Hydrogen can be injected either in the intake system or directly in the combustion chamber. Each technology is characterized by pros and cons significantly affecting the engine and the vehicle operation, which tailors the choice of the injection technology to the specific mission of the engine/vehicle.

Direct injection is preferable to limit the drawbacks caused by the low volumetric energy density of Hydrogen [15], as well as to reduce the risk of intake port backfire [16,17]. Conversely, PFI favours the homogenization of the mixture enabling an easier control of the combustion process and reducing the risk of NO_x production in rich-mixture pockets [18,19].

The typical wide range of ICE operations (in terms of load and revving speed) involves largely different scenarios for the injection time-window available to introduce the proper fuel quantity. Whenever high specific power is needed, high-pressure direct injection leading to supercritical conditions and under-expanded fuel jet is needed. Extensive research on this topic can be found in [20–22]: the supercritical condition leads to the formation of a well-known bell-shaped structure near the injector orifice, characterised by high Mach numbers. The first experimental outcomes were proposed back in the 1960s [23,24]. Subsequently, scientific literature has been enriched by years of publications using experimental imaging techniques [25], numerical simulations [26] or both [27]. Past and recent studies on under-expanded jets [28–30] have highlighted the complexity and importance of this phenomenon. Despite a large database of scientific studies has been made available in the recent past in the field of aerospace engineering for rockets, time- and length-scales typical of automotive fuel jets are largely different and therefore require dedicated work. Specifically, the interactions between the environment in the combustion chamber and the gaseous fuel have a notable impact on typical parameters measured under engine-like conditions, such as the jet penetration length and cone angle. Hence, a comprehensive experimental and numerical exploration is mandatory. In the field of automotive engineering, a number of gas characterizations in both critical and supercritical regimes has been performed at different pressure and temperature conditions, especially focusing on CNG [31,32]. More recently, interest has been quickly shifted towards Hydrogen, mainly in view of its carbon-free nature [33–36] as above commented. Wide ranges of injection pressures and design solutions have already been explored, covering LPDI (approx. 30–100 bar) and HPDI (approx. 100–300 bar) systems. Despite a key-role in mixture formation is expected to be played by the interaction between the relatively low-momentum fuel jet and the air motion in the combustion chamber, most experiments have been performed in quiescent chambers, to provide fundamental and detailed characterizations of the transient gas jet penetration and cone angle with optical diagnostics (i.e., Schlieren imaging in most cases) and mass flow rate evaluation. Such experimental campaigns provide very valuable datasets to validate numerical models, which in turn can be used then to perform sensitivity studies and injector design optimizations. Surrogate inert gases are commonly used in the experimental campaigns to mitigate issues related to unintended combustion and to reduce costs and complexities of the experimental setup. This is especially important when dealing with Hydrogen, due to its low ignition energy and light density, which necessitate special precautions to prevent gas leakage for safety reasons. Hydrogen’s peculiar properties make the selection of an appropriate inert gas for experimental campaigns challenging, when seeking accurate characterization of Hydrogen injectors. Argon (Ar), Nitrogen (N_2), and Helium (He) are widely employed as inert gas surrogates in Hydrogen jet studies. However, the influence of varying gas properties on experimental outcomes remains insufficiently understood, primarily due to the lack of a systematic experimental campaign conducted under controlled and consistent conditions. The present work addresses this gap by providing a detailed characterization of a LPDI injector operated with the aforementioned inert gases under two distinct operating regimes, using identical hardware throughout and following the same procedure discussed in [37]. The injector is a single-hole prototype unit provided by Marelli Motorsport, which is analysed both experimentally and numerically in a quiescent chamber filled with air at ambient pressure and temperature. Inert gaseous species progressively closer to Hydrogen are tested and the resulting dataset enables a thorough comparison of the jet characteristics across different gases and serves as a validation benchmark for a numerical 3D-CFD framework developed to replicate the behaviour of gas jets under varying injection conditions. The validated model offers a robust tool to select the most appropriate surrogate gas. Indeed, numerical simulations are applied to extrapolate the behaviour of the investigated injector under Hydrogen operation enabling the direct comparison between the gases thereby minimizing the need for expensive and potentially hazardous experimental testing with Hydrogen.

The structure of the paper is as follows: in the next paragraph, the experimental setup and test matrix is presented. Then, the numerical setup is discussed. The comparison between the experimental and numerical outcomes is then carried out in the result section: focus is initially made on the steady flow operation of the wide-open injector position; subsequently, the comparison is extended to cover a fully transient engine operation including the ballistic injector opening phase. Remarks are then made to emphasize the good agreement between the experiments and the developed numerical approach, as well as its general validity across different gases and injector operations. Finally, conclusions are drawn to identify the best gaseous candidate to consistently replace Hydrogen in the experimental tests.

2. Experimental setup

This section presents the two experimental techniques used to provide the validation data for the numerical/experimental comparison. Specifically, Schlieren imaging is applied to visualize the primary Mach cone under steady-state conditions. Additionally, transient high-speed imaging acquisitions are conducted to comprehensively assess the behaviour of the gas-jet throughout its temporal and spatial trajectory. Instantaneous needle lift is simultaneously measured during the tests using Laser-Doppler Vibrometry, providing valuable input data for the transient numerical simulations. A Coriolis-type mass flow meter is used to determine the mean injected quantity in each tested operating conditions. This preliminary experimental phase is aimed at characterizing the jet behaviour for various inert gases, to validate a numerical setup capable of accurately reproducing the behaviour of generic injected gases under actual injection conditions, thus providing the ideal pathway to the investigation of Hydrogen jets.

2.1. Schlieren imaging technique

The Schlieren technique enables the visualization of gases in air by exploiting the variation of refractive index n in the examined flow field. At the interface between different gases, characterized by different refractive indexes, light beams are refracted altering their path with respect to the incident light direction. Using a “knife blade”, i.e. a sharp-edged obstruction, the light beams not deviated by the refraction mechanism are stopped intensifying the visualization of gaseous jets in the surrounding air. Gladstone-Dale’s law [38] relates the refractive index of a fluid to its density as reported in Eq. (1):

$$n - 1 = k\rho \tag{1}$$

where the Gladstone-Dale’s coefficient k depends on the injected gas and on the wavelength λ of the light source. The link between the capability to observe a gaseous jet in air in each position and the local values of its density, pressure, temperature is evident. In the case of Helium, which has a significantly different density from the surrounding air, this results in a pronounced refractive index gradient enabling a clear visualization of the jet. However, the same is less true for gases like Argon and Nitrogen, which have densities comparable to the surrounding air. When gases have comparable densities at standard conditions, the visibility of the jet depends largely on its velocity. This results in a highly visible jet near a high-pressure injector orifice, where velocities are extremely high, while a clear detection at larger distances becomes increasingly challenging.

To reduce inaccuracies in assessing the jet characteristics, such as its shape and morphology, the Schlieren analysis outcomes should be sided by additional techniques, such as the local momentum flux measurement, which may help to assess variations in terms of cone angle for different gas species [39–42]. While such additional techniques are not reported in the present work, they are being currently investigated and they will be the object of future investigations.

2.2. Laser-Doppler Vibrometry technique

Laser Doppler Vibrometry (LDV) is a contactless measurement technique capable to evaluate the displacement of a moving object as a function of laser light frequency variation, involving Doppler effect. A vibrometer is composed by an optical part, formed by a laser source and an interferometer, and an electronic part which elaborates the photodiode output signals. When a relative motion between the interferometer and the moving surface occurs, a Doppler effect is detected, i.e. the frequency of the light beam reflected by the moving surface changes. From the measurement of the frequency variation, it is possible to calculate the relative velocity between the instrument and the moving surface, being in the present case the back surface of the injector needle. Time integration of the velocity signal provides the relative displacement. This information is then provided as an input to the unsteady 3D-CFD simulation of the injector operation.

2.3. Schlieren optical bench

The tested injector is a research LPDI unit derived from a GDI injector manufactured by Marelli Motorsport. In order to obtain data pertaining to a linear flow configuration, interactions between adjacent jets are excluded using a single jet structure: the injector presents a single cylindrical hole coaxial to the injector axis, with a diameter of 0.65 mm. The injector is controlled through a peak-and-hold current signal managed by an AEA A006 programmable driver. The system is fed by three different gases: Argon (Ar), Nitrogen (N_2) and Helium (He), each supplied with dedicated 200-bar cylinders. A pressure regulator is used to obtain the required supply pressure following the operating conditions presented in Table 1. A Coriolis-type mass flow meter (Siemens Sitrans Mass2100 DI1.5) and a 30 cc volume (rail in the following) are placed upstream of the injector. The rail is instrumented with a Keller PAA-M5-HB pressure sensor and a k-type thermocouple. Moreover, a PID-regulated heater is placed over the rail surface to control the gas temperature. The injector-rail system is installed on the top of a vessel designed to operate up to 12 bar backpressure and up to 100 °C ambient temperature. The vessel has three side optical accesses, oriented at 90° one to each other, with a diameter of 100 mm. The Schlieren optical system, used for the jet characterization, is arranged in a classical “Z-configuration” schematically shown in Fig. 1.

The optical line presents a Luminus CBT-140-W led, used as point light source. The light beams are parallelized with a first Edmund Optics 60″ focal length parabolic mirror. A second twin mirror is used to refocus the beams on the knife blade. The test chamber is placed in the centre of the region between the two mirrors. The vessel is oriented to have two optical accesses in line with the light collimated beam. Gas jets are evaluated both in steady-state and dynamic conditions. In the first case, to increase the resolution of the Mach disk and cone images, a 4 Mpixel Jay TM-4200C Fast Shutter Camera (FSC) is used with 20.0 μs exposure time. For the transient operations, a High-Speed Video (HSV) Phantom Vision Research 7.10 camera is used. For HSV, 592 × 208 pixel resolution, 50000 Hz frame rate and an exposition time of 1.0 μs are set. Both cameras are equipped with a 200-mm Nikkor objective. With this equipment, a spatial resolution of 6.462 pixel/mm for the HSV and 17.436 pixel/mm for the FSC are obtained respectively.

2.4. Laser-Doppler vibrometer bench

The needle lift time-history is provided as input for the unsteady CFD simulations. The injector in the fluid inlet is devoid of the filter, making the needle optically accessible from the back. In the present injector mechanical design, the anchor is rigidly connected to the needle, hence the needle displacement can be measured from the fuel inlet in the back of the injector body using a laser doppler vibrometer. For this measure, the rail-injector system is equipped with a quartz optical access positioned on-axis with the injector, while the gas is supplied by a side access to the rail. A Polytec NLV – 2500 laser doppler vibrometer is used for the measurements. The laser beam is aligned by means of a 3-axis micrometric positioning system, in order to be incident to the back of the needle. Details of the test assembly [40] are illustrated in Fig. 2.

2.5. Test plan

In the present section, the experimental test plan is presented. Each test is carried out by analysing three progressively lighter gas species: Ar, $N_2$and He. As a preliminary measure, the mean injected mass per injection event is measured using the Coriolis-type mass flow meter

Table 1
Test plan of numerical/experimental analysed cases.

Test	Injected gas	P_{inj} [bar,a]	T_{inj} [K]	P_{vessel} [bar,a]	P_{inj}/P_{vessel}	ET EMI [ms]	ET Imaging [ms]	ET Needle Lift [ms]
Case A	Argon (Ar), Nitrogen (N_2), Helium (He)	40	298	1	40	0.33 to 6	5	1.5
Case B		20	298	1	20	0.33 to 6	5	1.5

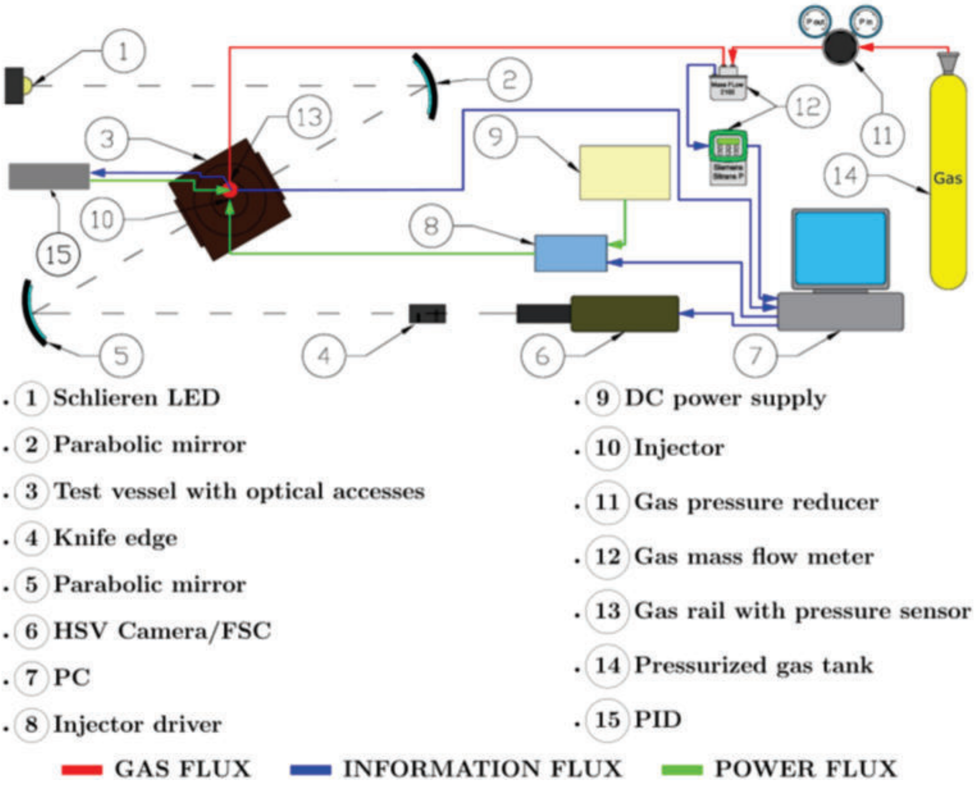

Fig. 1. Experimental layout of the test bench.

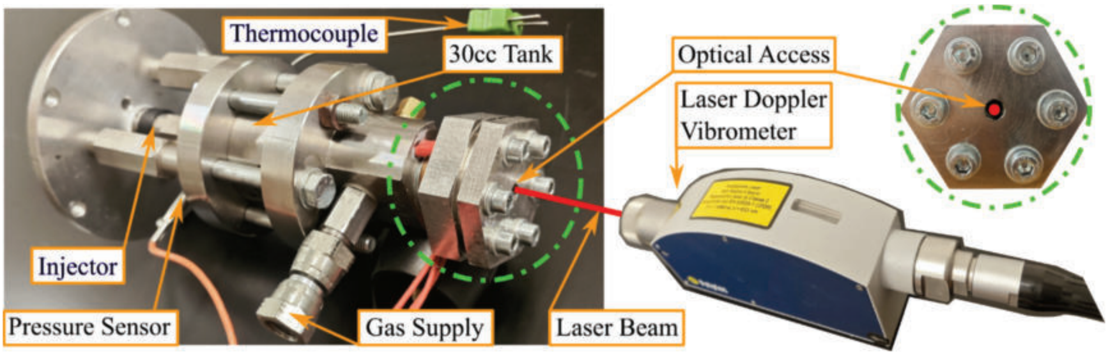

Fig. 2. Laser-Doppler Vibrometry system layout.

resulting in EMI curves for each gas. The excitation time (ET) in this instance ranges from 0.33 to 6.0 ms with a working frequency of 10 Hz. For both stationary and transient image analyses, the ET is set to 5.0 ms to ensure the achievement of a fully developed jet structure. A total of 20 images are acquired for each condition in both cases. Finally, for needle lift measurements, an ET of 1.5 ms is selected to reduce the computational cost of the numerical simulations. The operating conditions are shortly reported in the following Table 1.

2.6. Imaging post-processing algorithm

For HSV frames post-processing, a jet contour detection software, based on Simple Standard Deviation algorithm [43] was developed in the LabVIEW® environment. The images captured just before the appearance of the jet are used as background. The software executes a 7-step procedure reported below and depicted in Fig. 3:

1. Gaussian smoothing filter application both to the background and to the jet images.

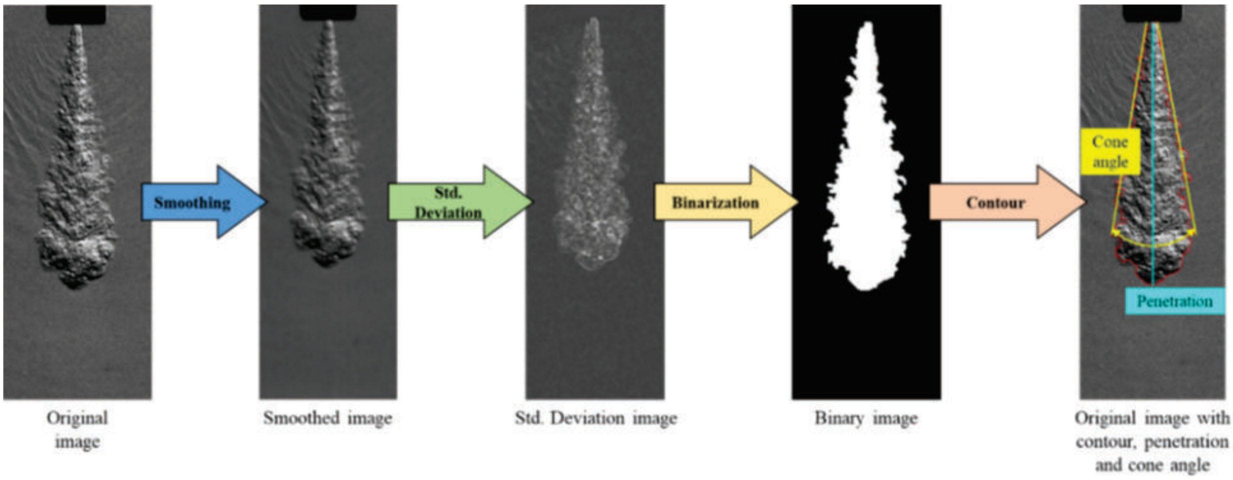

Fig. 3. Jet identification through edge detection process.

2. Smoothed images (jets and background) sub-sampling, with the use of small square subsets.
3. Computation of the standard deviation of pixels grey levels in each subset and construction of an auxiliary standard deviation matrix.
4. Subtraction between the jet standard deviation matrix and the background one.
5. Application of a threshold value to binarize the image resulting from the subtraction step.
6. Identification of the binary image contour.
7. Calculation of penetration and cone angle: maximum jet tip distance to nozzle and opening angle.

3. Numerical setup

Steady state and transient simulations are performed with Simcenter STAR-CCM + licensed by SIEMENS DISW (v2310) in a RANS (Reynolds Average Navier Stokes) environment. Taking the advantage of the symmetry of the analysed nozzle tip, a reduced portion of the actual geometry, i.e. a 36° sector corresponding to 1/10 of the real one, is simulated. Aside from the nozzle tip, the numerical domain includes a cylindrical vessel of 30 mm radius and 100 mm length in which gases are injected.

The CFD ambient size and shape are different from the experimental vessel ones to reduce the computational cost of the simulations; nevertheless, an "open" constant pressure ambient is considered applying pressure boundary conditions to the CFD domain borders, exception made for the symmetry planes. A pressure boundary conditions is also applied upstream the nozzle tip to match the experimental pressure ratio. In particular, a nominal value of 40 and 20 bar is considered for Case A and Case B respectively, neglecting instantaneous pressure oscillations in the injection apparatus, which are deemed to be negligible. A constant value of 298 K is imposed at the inlet for temperature. A schematic of the simulated computational domain and applied boundary conditions is reported, for the sake of clarity, in Fig. 4.

Following previously performed sensitivity and validation studies on the same injector [37] the AMR (automatic mesh refinement) technique is replaced by a fixed mesh refinement strategy. A polyhedral mesh with a base size of 1 mm is generated refining the grid near to the nozzle tip and in the region where the Mach cone develops. A cylindrical refinement region with a mesh size of 10 μm is placed to refine the needle curtain while 3 cones with progressively lower height and radius are considered to refine the mesh in the vessel. The cell size in the conical refinements VC1, VC2 and VC3 represented in Fig. 5 is 160 μm, 80 μm and 40 μm respectively, leading to a 160 μm maximum cell size in the region of interest.

To ensure a y+ value lower than unity, 10 to 15 prismatic layers are applied at the tip, needle and nozzle walls. The number of layers, their total and near wall thicknesses are adjusted for each case to match the target y+ value while avoiding too high prism layer stretching, lowering the quality of the mesh.

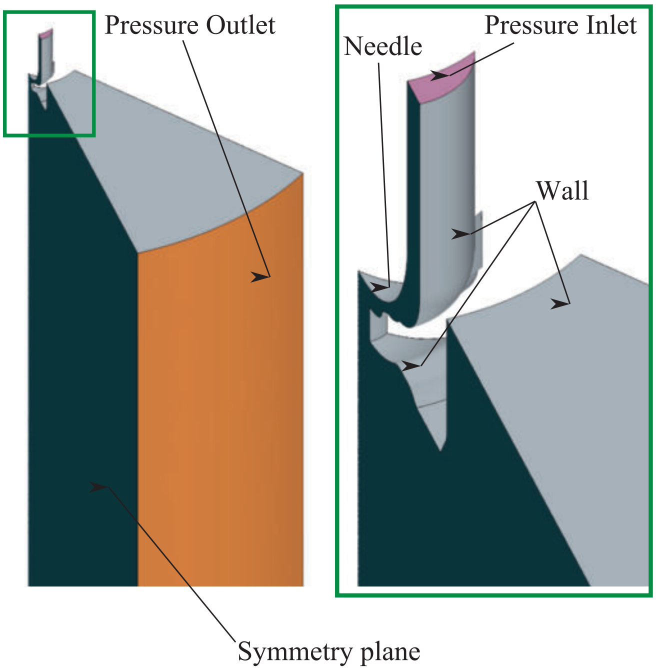

Fig. 4. Schematic of the simulated domain and boundary conditions specification.

In transient simulations, the needle lift is accounted for trough a morphing-and-remesh strategy: a displacement condition is applied to the tip according to the measured needle lift law; the grid is then morphed to follow the needle displacement. To avoid excessive degradation of the mesh quality, remeshing events are automatically triggered when the node displacement becomes too high with respect to the initial (unmorphed) position. The solution is then re-mapped onto the new grid and the simulation proceeds. An example depicting the curtain mesh evolution during the needle opening phase is reported in Fig. 6, where the 4 considered timings correspond to the starting position (non-zero initial lift), 25 %, 50 % and 100 % of the actual (maximum) needle lift.

A 2.5 % of the maximum lift is selected as a trade-off between simulation accuracy and mesh quality for the non-zero initial needle lift.

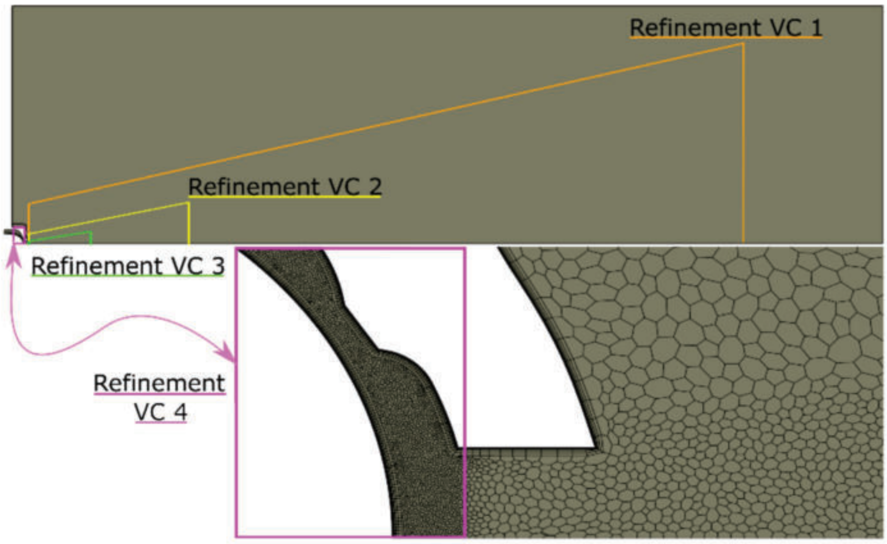

Fig. 5. Domain overview and refinements volumes control with a focus on needle and under-expanded zone.

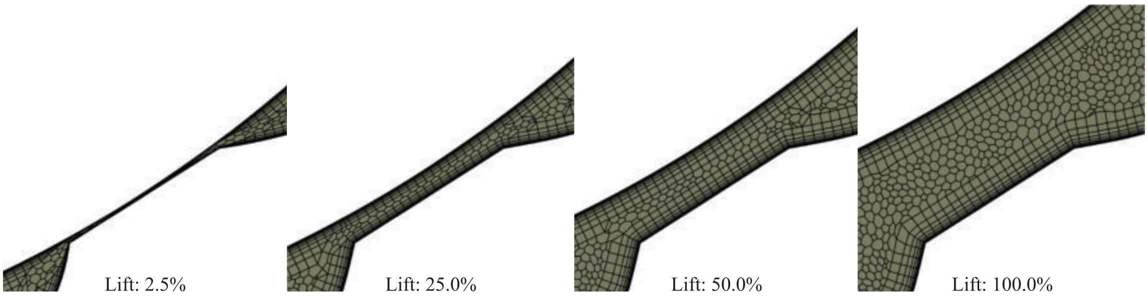

Fig. 6. Temporal evolution of the curtain mesh during the needle lift transient.

The experimental needle lift law is therefore modified accordingly applying a time-shift of 290 µs; furthermore, measured oscillations in the needle stationary phase are removed (Fig. 7); finally, the same maximum lift is applied in both transient and steady state simulations. The adopted meshing strategy results in a maximum number of cells around 2.5 million, which allows the simulation to cover the desired time frame in about 24 h with the following computational resources:

- 20 CPUs for the steady state simulations
- 208 CPUs for the transient simulations (considering 30 remeshing events, a total physical time of 750 µs, with a numerical time step from 1.0e-8 s to 5.0e-8 s)

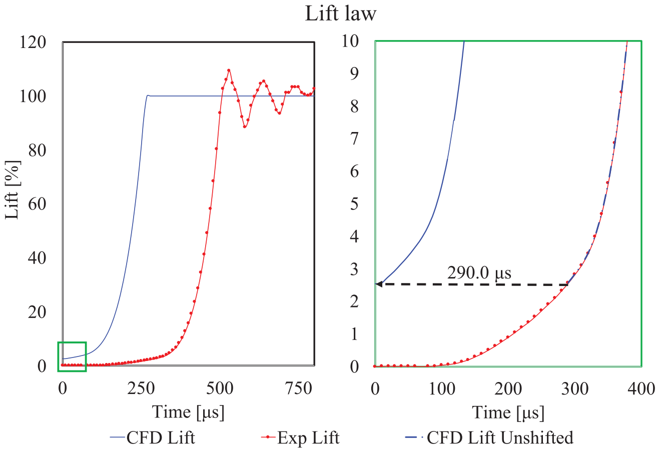

Fig. 7. Comparison of normalized measured and CFD needle lift law.

Considering the specific goal of the study, special attention is paid to define both the background and the injected gas properties. The specific heat of each gas is prescribed as a function of temperature trough NASA polynomials, while the Sutherland's law is applied for dynamic viscosity. The molecular diffusivity is defined trough the "kinetic theory" starting from Dipole momentum, Lennard-Jones characteristic length and energy as a function of absolute pressure and temperature. A similar approach is adopted for thermal conductivity, using the Mathur-Saxena averaging method for the mixture property. A mass weighted average is considered for mixture specific heat and dynamic viscosity. The applied methods and parameters are summarized in Table 2 for all the involved gases.

The Soave – Redlich – Kwong real gas equation of state [44] is applied instead of the widely adopted ideal gas formulation considering the peculiar values of pressure and temperature reached in under-expanded gas jets. Furthermore, a coupled flow solver (CF) is used instead of a segregated one (SF): mass and momentum equations are therefore considered as a system (w/o using predictor–corrector to establish the link between mass and momentum equations) and solved simultaneously. While such choice requires higher computational time and memory, it increases robustness, and it is highly recommended for highly compressible fluids involving shock wave phenomena, such as the considered one. A second order discretization scheme is adopted for flow, energy, species and turbulent quantities while following the sensitivity study reported in [41] the Realizable K-ε turbulence model is

Table 2
Gases thermophysical properties.

	Ar	N_2	He	H_2
Specific Heat	NASA Polynomial			
Dynamic Viscosity	Sutherland's Law Ref: 2.125e-5 Pa •s Constant: 114 K Ref. T: 273 K	Ref: 1.716e-5 Pa •s Constant: 111 K Ref. T: 273 K	Ref:1.870e-5 Pa •s Constant: 79.44 K Ref. T: 273 K	Ref:8.41 e-6 Pa •s Constant: 97 K Ref. T: 273 K
Thermal Conductivity	Kinetic Theory			
Molecular Diffusivity	Kinetic Theory			
Critical Temperature [K]	150.86	126.2	5.2	33.23
Critical Pressure [Pa]	4.898E+06	3.400E+06	0.227E+06	1.316E+06
Lennard-Jones characteristic Length [A]	3.33	3.621	2.576	2.92
Lennard-Jones Energy [K]	136.5	97.53	10.2	38
Molecule Type	Atom	Linear Molecule	Atom	Linear Molecule

selected for the present work.

4. Results

This section provides an overview on the experimental and numerical results and their comparison. It is divided in three subsections: the first one presents an assessment of the experimental results, in the second and third numerical steady and unsteady outcomes compared to the experimental ones are showed.

4.1. *Experimental results*

As a preliminary step, the injector was characterised by fluxing it using different gases. A Coriolis mass flow meter was used for this purpose, acquiring the mean mass flow rate; further the current profile, the needle lift and the pressure time-history in the rail were recorded in each operating condition. As an example, in Fig. 8 the current profile, the needle lift, and the pressure profile are reported for a 1.5 ms ET injection event.

As can be observed in Fig. 8, the presence of the 30-cc-volume tank in the injector inlet allows a moderate drop for the supply pressure of about 0.35 bar. The actual start and end timings of the gas outflow can be detected by a change in the slope of the pressure curve and by the needle lift curve. Compared to the electric command signal, there are delays in the start and in the end of the flow of about 0.5 ms and 0.75 ms respectively, caused by the inertia of the needle and fluid, resulting in an actual duration of the injection process of about 1.75 ms.

The mass flow rate analysis results are presented in Fig. 9, illustrating the measured mean mass per shot and mean volume per shot for Ar, $N_2$and He and an extrapolation of the same quantities for H_2. The curves were obtained by varying the ET between 0.33 ms and 6 ms. In every instance, a ballistic region exists for ET values shorter than 0.5 ms which pertains to the opening transient of the injector. For higher ET values, the injector's behaviour becomes linear. The volume flow rate was derived by the measured mass flow rate considering the upstream (rail) conditions. For all the tests, the injection pressure exceeded the critical condition, resulting in the injector operating under supersonic flow conditions and elaborating the choked mass flow rate.

By comparing the flow test results of the different tested gases, the dependence of the injector behaviour in terms of injected mass from the used gas properties (k ratio of specific heats and R constant) is confirmed in each operating condition (injection pressure and rail temperature).

Table 3 reports the gas constant (R) and (k) value, the critical velocity (c^*) and the density value corresponding to the upstream conditions (ρ_0). Further, the same Table 3 reports the measured static mass flow rate of the injector (MFR,exp) in the different cases (gas and injection pressure) derived from the EMI curves as the mean value obtained for the different ET pairs in the linear zone (ET greater than 1 ms). The discharge coefficient (C_d) of the injector in steady flow conditions was evaluated as the ratio of the measured mass flow rate to the theoretical mass flow rate value (MFR,th) obtained via the flow equation under choked conditions using the nominal nozzle hole area as reference (Eq. (4)). As reported in Table 3, the discharge coefficient shows only minor variations in the examined conditions (2 %–4 % for Case A and 4 %–7 % for Case B). By assuming as repeatable the injection rate behaviour during the transient phase (opening and closing) and considering the moderate variation of the discharge coefficient, it is possible to scale the EMI curve of a gas species in another starting from the corresponding ratio of the chocked flow rates (Eq. (4)). Therefore, an extrapolation of the results for H_2using the three tested gases as

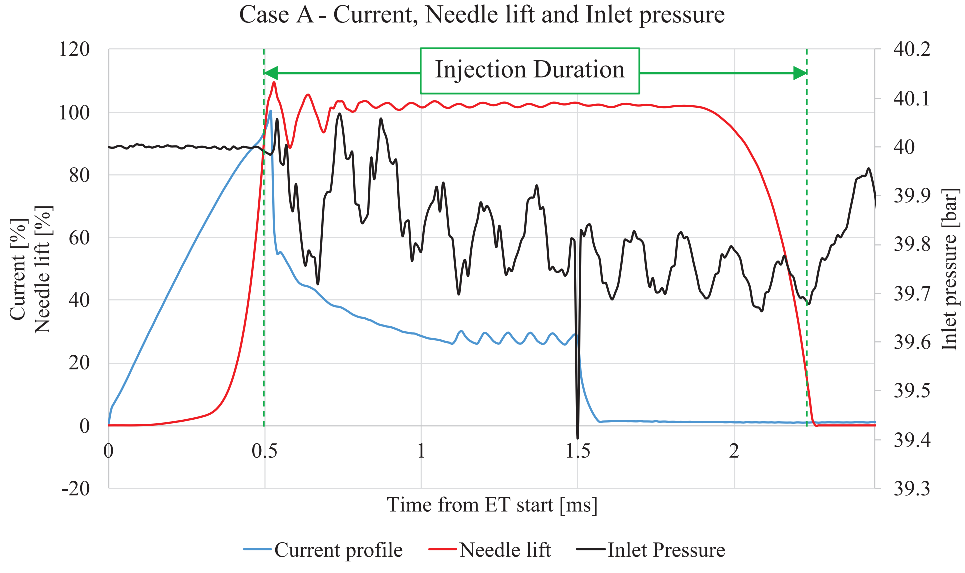

Fig. 8. Current pilot, needle lift and pressure inlet profiles.

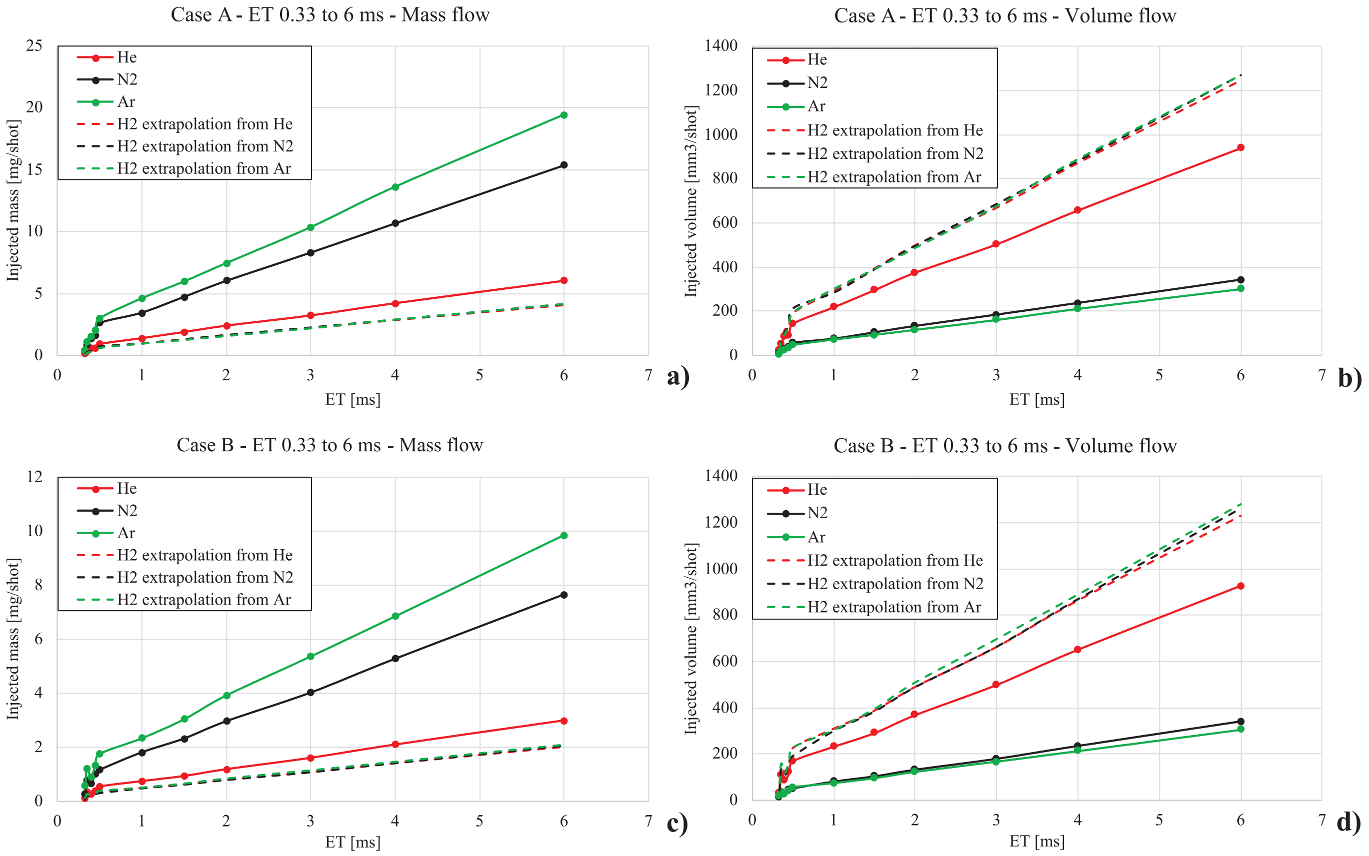

Fig. 9. Experimental and H_2-extrapolation of mass and volume flow rate of different gases in Case A and B.

Table 3
Overview of experimental results in steady-flow condition.

Case	Gas	R [J/kmol°K]	k [n.d.]	c* [m/s]	ρ_0 [Kg/m3]	MFR,exp[g/s]	MFR,th [g/s]	C_d [n.d.]
A	He	2077.1	1.667	879.9	6.459	0.950	1.225	0.776
	N_2	296.8	1.400	321.3	45.204	2.428	3.055	0.795
	Ar	208.1	1.667	278.5	64.463	2.950	3.870	0.762
B	He	2077.1	1.667	879.9	3.229	0.447	0.612	0.730
	N_2	296.8	1.400	321.3	22.602	1.160	1.528	0.759
	Ar	208.1	1.667	278.5	32.231	1.516	1.935	0.784

reference (dashed plots in Fig. 9) was proposed.

$$\dot{m} = A_{nom}\sqrt{P_0 \bullet \rho_0 \bullet k \bullet \left(\frac{2}{k+1}\right)^{\frac{k+1}{k-1}}} \tag{4}$$

From the contour of the jet images for the different gases, obtained by HSV, the penetration and cone angle curves for cases A and B were derived (mean over 20 acquisitions, along with the respective standard deviation for each timing). Results are reported in Fig. 10, in which a) and b) are related to Case A while c) and d) are related to Case B. As can be seen in Fig. 10, both for Case A and Case B, He jet is more penetrating and has a larger final cone angle than Ar and N_2. In the right plots, a comparison is reported in terms of relative differences for the same quantities.

In terms of jet tip penetration, discrepancies among the different gases were evaluated respectively from 400 to 1000 μs for Case A and 400 to 800 μs for Case B. The difference in the considered timings is due to the less evident gas plume structure for the Case B conditions, in which the jet can hardly be recognized in the images (particularly for N_2 and Ar) well downstream the nozzle, were an intense dilution with the surrounding air was attained. The same comparison is carried out in terms of jet mean cone angle, averaged over the 600 to 1000 μs time-window for Case A and from 600 to 800 μs for Case B.

The relative difference in terms of penetration among He and the other two gases decreases during the injection event, suggesting a more evident depletion in the He jet tip velocity after an initially faster jet development with final tip velocity values being around 65–70 m/s for the different gases used as test fluid. The observed longer penetration and the correspondingly higher He cone angle are the result of the greater volumetric flow rate in the discharging conditions and of the higher velocity at the orifice outlet section, with globally a significantly larger jet structure for He at any given timing.

4.2. CFD results – Steady state simulations

Steady state simulations are performed following the previously described methodology. i.e. fixing the needle tip position to the maximum nominal value and superimposing a pressure ratio of 40 bar for Case A and of 20 bar for Case B.

For each operation, the experimental sensitivity analysis to the injected gas is numerically reproduced, adding a fourth case to simulate the impact of inert gases replacement with H_2. To check the reliability of

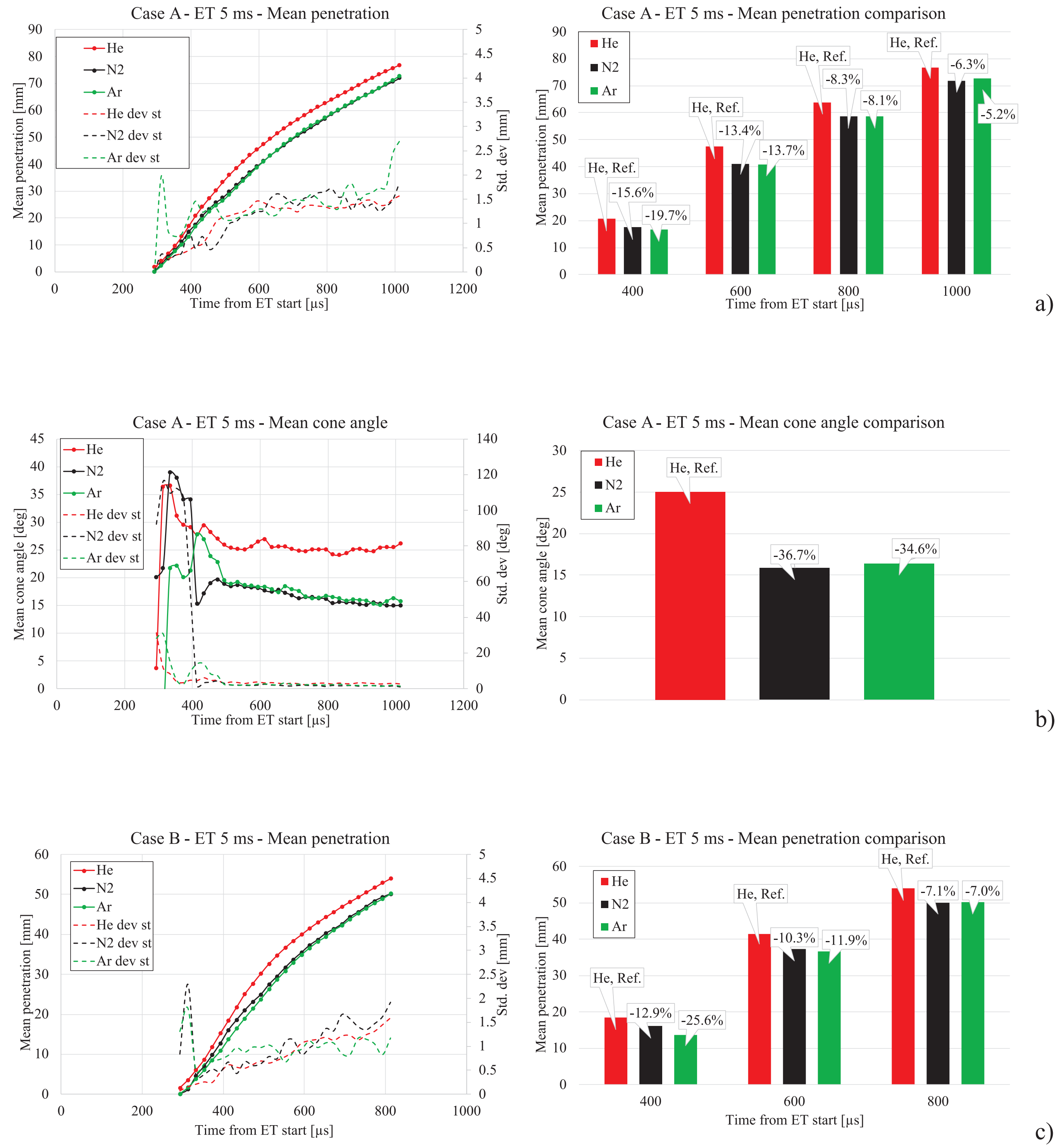

Fig. 10. Penetration and cone angle curves and relative comparison of He, N_2 and Ar for both case A (a, b) and B (c, d).

the proposed methodology, the measured and simulated mass flow rates are compared in Fig. 11. The simulations can reproduce the mass flow reduction as a function of the injected gas density with a relative error in between 1.5 % and 7.5 % (average 4.1 %).

Applying the nominal pressure ratio the CFD model always overpredicts the mass flow rate with respect to the measured value; this is reasonably in line with the (even if small) reduction of the inlet pressure during the injection event which is not accounted for in the steady-state CFD framework. An almost constant discharge coefficient (0.786–0.808) is found comparing the theoretical mass flow rate and the calculated one confirming the low sensitivity to the injected gas. The above result is still valid also when injecting H_2: a 0.80 C_d is calculated with both pressure ratios. The linear dependence of the mass flow from the reference gas density square root is well verified by the CFD results, as reported in Fig. 12 for both operating conditions.

The numerical results are further analysed to deepen the comparison between the injected gases by monitoring the main characteristics of the exiting column close to the nozzle. Maximum velocity, Mach number

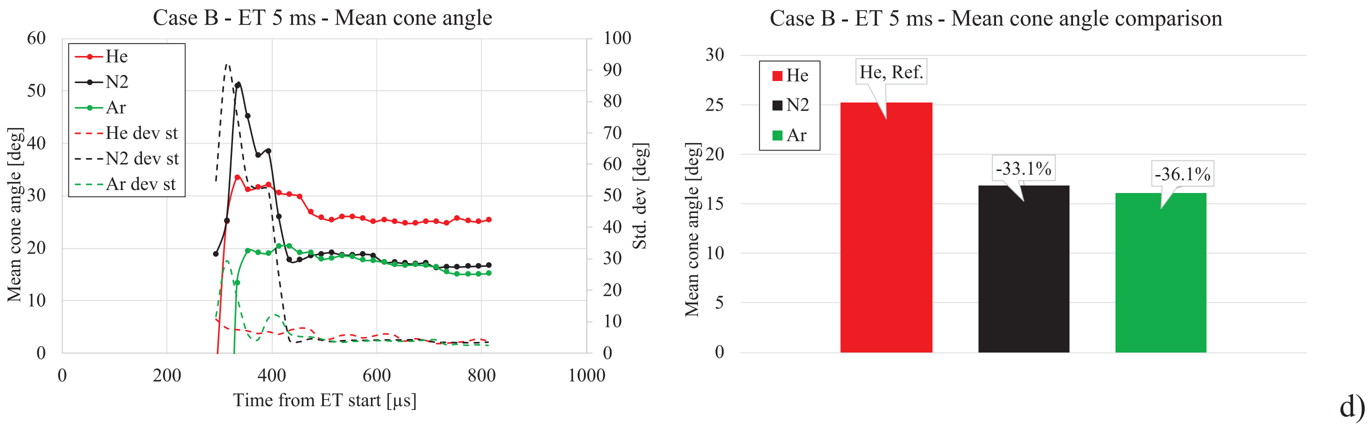

Fig. 10. (*continued*).

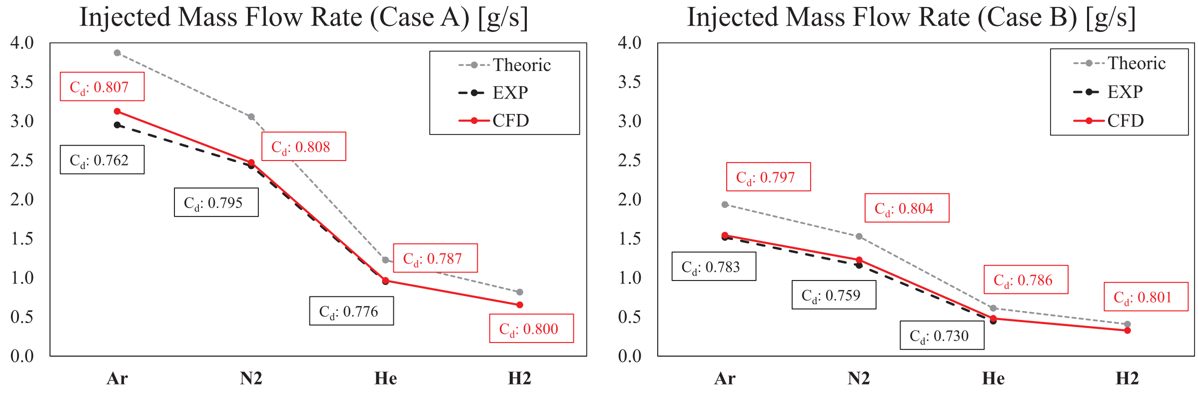

Fig. 11. EXP/CFD comparison of static mass flow rate changing the injected gas in Case A (left) and Case B (right).

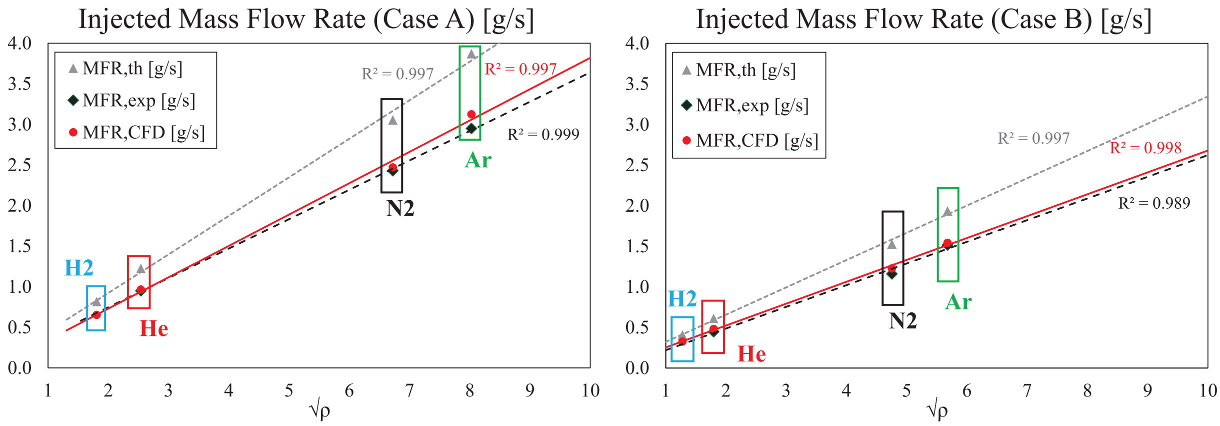

Fig. 12. Theoretical, Experimental and Calculated injected mass flow rate as a function of the reference gas density square root for Case A (left) and Case B (right).

and minimum temperature/pressure in the expansion region are monitored and reported in Table 4. The maximum gas velocity is only slightly affected by the change in the pressure ratio while it is highly impacted by the selected gas, with a gas velocity for the H_2 case almost 5 times higher than the Ar one. Despite the relatively similar density, a 60 % higher maximum velocity is found comparing H_2 to He. Such difference is deemed to be when approaching transient simulations, due to more stringent time-step requirements when simulating the injection of low-density gases in under-expanded conditions.

Reducing the pressure ratio, the minimum temperature in the under-expansion region rises, thus increasing the local speed of sound. As a consequence, the maximum Mach number reduces comparing Case A and B despite similar gas velocities. Differences in the gas properties (R and k) and in the local speed of sound lead to different trends comparing the maximum Mach number reached with different gases: almost the same value is detected comparing bi-atomic gases with mono-atomic ones (N_2/ $H_2$with respect to Ar /He). The same trend is found comparing the minimum temperature and pressure values. The scalar fields of velocity, Mach number, absolute pressure and temperature in the under-expansion region are reported for all the considered cases in Fig. 13. Except for the velocity, showing an always increasing trend moving from high-to-low density injected gas, almost superimposed scalar fields are detected comparing Ar/He and N_2/H_2 under both simulated operations (Case A and B).

Table 4
Simulated main physical quantities in the first Mach disk region.

Case	Gas	Max. Velocity [m/s]	Min. Temperature [K]	Min. Abs. Pressure [Pa]	Max. Mach [-]	Speed Of Sound [m/s]
A	Ar	532	12	1530	8.4	65
	N_2	725	35	2580	6.0	121
	He	1724	12	1500	8.4	206
	H_2	2737	35	2550	6.1	450
B	Ar	532	20	2210	6.5	83
	N_2	713	48	3490	5.1	141
	He	1700	20	2248	6.4	264
	H_2	2668	47	3361	5.1	522

Relevant differences are found when comparing the shape of the shock wave region changing the pressure ratio, with a general reduction of the distance from the nozzle of the first Mach disk when reducing the injection pressure. Comparing the gases, despite the axial position of the Mach disk is almost constant for both operations, differences can be noticed in terms of radial width of the bell-shaped region: the width is generally higher with N_2 compared to Ar and He.

A close-up of the Schlieren acquisition can be compared with the density gradient magnitude field resulting from the CFD simulations to check the reliability of the numerical results. From both experiments and CFD it is possible to extract three characteristic lengths to characterize the Mach disk morphology, the first quantifying the distance at which first shock wave occurs (L1) and the other two quantifying the width of the barrel (L2, L3) as schematically reported in Fig. 14. From a graphical comparison of the Mach disk shape the wider structure of Ar compared to N_2 is visible in both experiments and simulations, qualitatively confirming the reliability of the performed simulations; conversely, the similarities between Ar and He cases are less evident from the optical acquisition partly due to the lower quality of the experimental images with He as a gas.

An overall comparison between experimental and CFD characteristic lengths is shown in Fig. 15, quantitatively reporting the change in the Mach disk shape changing the pressure ratio and the injected gas. The reduction of L1 and of the disk width reducing the pressure ratio is correctly represented by the simulations across the investigated gases. In the experiments, a reduction of the L1 length is visible moving from Ar to N_2 while a flat value is measured comparing He with N_2. This trend is not correctly reproduced by the CFD model, which predicts an almost constant L1 for all the gases.

Despite some misalignment in the axial length prediction, the relative trend for the radial disk width changing the gas is well represented by CFD, and similarities between Ar and He with respect to N_2 are confirmed, this last showing the highest width in both operations.

The model accuracy in predicting the Mach disk morphology can be considered satisfying, given an average relative error lower than 10 % across the tested conditions. This is further supported by the difficulties in exactly measuring the characteristic lengths from the experimental images (especially for He) and the however present shot-to-shot variability.

Some conclusions on the shape of the Mach disk in case of H_2 injection can be drawn analysing the CFD results, confirming the previously noticed similarities with N_2 characteristic lengths. This corroborates the primary role of the molecule structure (mono/bi atomic) in shaping the Mach disk with respect to gas density, and it suggests the suitability of N_2, instead of He, as a candidate surrogate gas for H_2 if focus is made on flow details in the near nozzle region. The overall picture in comparing Schlieren images and CFD results is reported for the sake of completeness in Appendix A for H_2 case also.

The wider under-expansion region could suggest an increase of the jet cone angle when injecting N_2 and H_2 with respect to Ar or He. This is

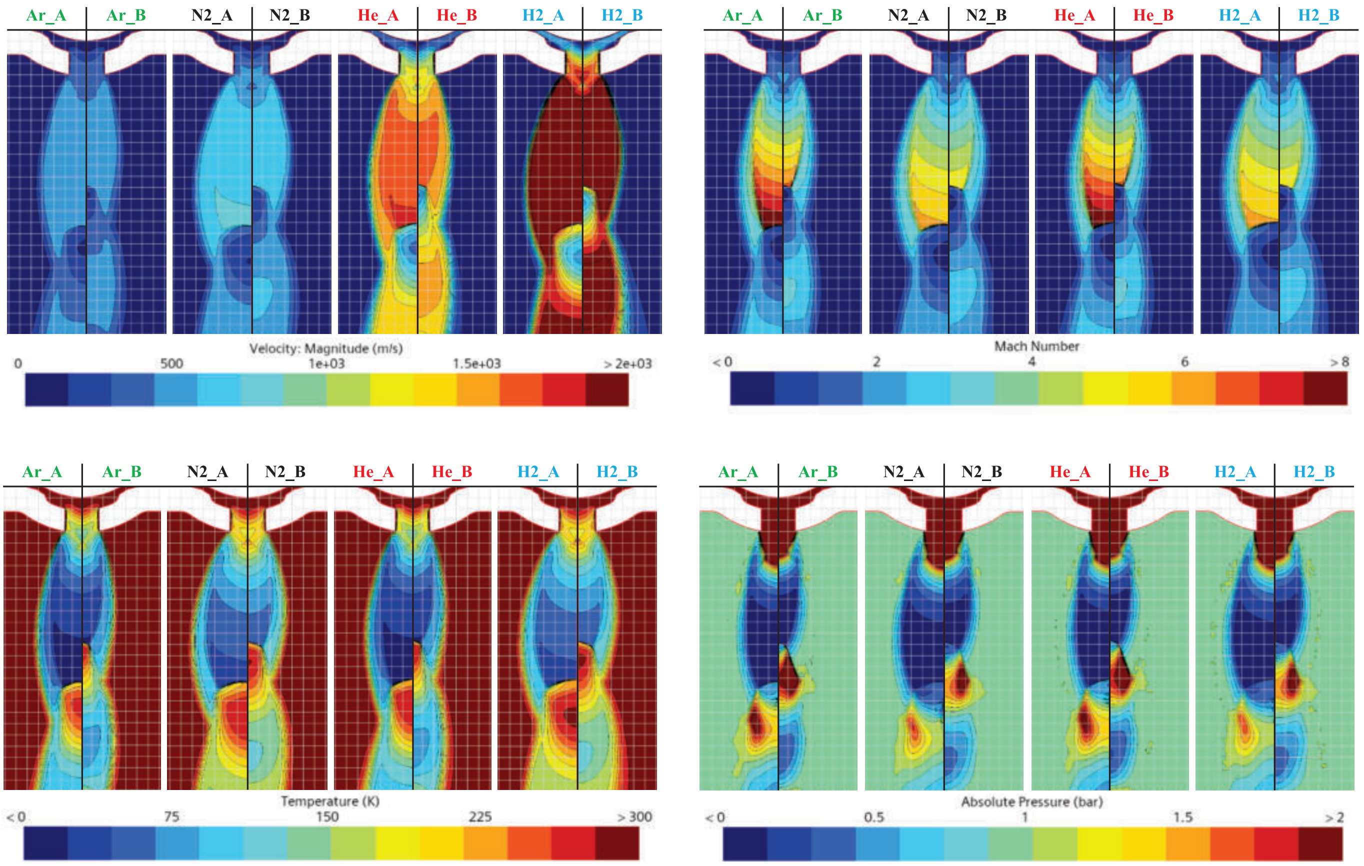

Fig. 13. Scalar fields of Velocity magnitude, Mach Number, Temperature and Absolute pressure for all the considered cases in the under-expansion region.

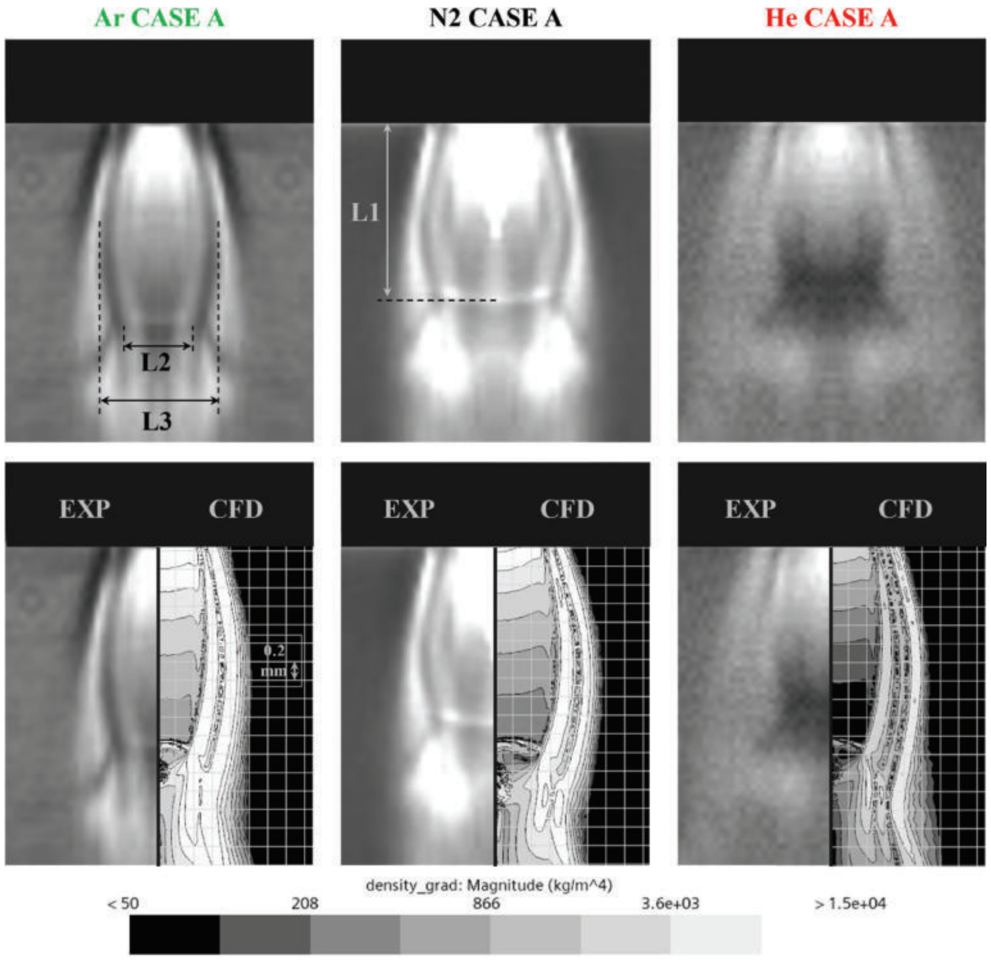

Fig. 14. EXP/NUM comparison on the main Mach disk cone on Case A operating condition.

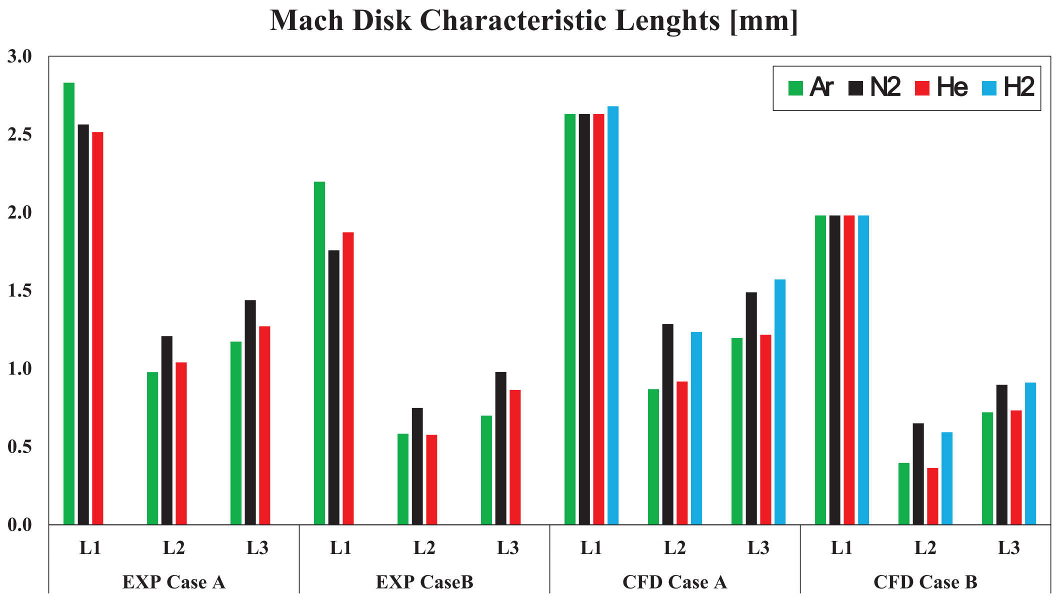

Fig. 15. EXP/CFD comparison of Mach Disk characteristic lengths in Case A and Case B.

not verified analysing the measured data, which show almost superimposed results for Ar and N_2 and increased penetration and cone angle with He. A weak relation between the Mach disk morphology and the main jet characteristics far away from the nozzle tip is therefore suggested, where probably mixing and diffusion mechanisms of the injected gas with the surrounding air play a dominant role.

In a steady-state framework it is not possible to infer how the jet penetration will evolve in time when changing the injected gas properties. Yet, some considerations on the cone angle can be made visualizing the jet at stabilized conditions. Images of the jet shape in Case A are reported in Fig. 16.

The gas jet the density gradient is considered applying the same logarithmic scale as in the previous analyses. To separate the jet from the background, a transparent color is applied for a density gradient lower than 50 kg/m^3 and the same threshold is applied in all the cases. The cone angle is computed measuring the jet width at 40 mm distance far from the nozzle tip. As clearly noticeable in Fig. 16, despite Ar and He show similar width of the first Mach, a different jet shape is found. Lower cone angles are found for Ar and N_2 compared to He and H_2. This result, which is in line with the experimental cone angle measurements during transient operation, further confirms the weak relation between Mach disk width and jet cone angle in stabilized jet conditions. Focusing on the H_2 jet shape, it is surely closer to the He one despite the previously commented similarity with N_2 for the Mach disk region: a marginal increase of the cone angle is detected when injecting H_2 with respect to He.

4.3. CFD results – Transient simulations

To further assess the reliability of the CFD model to predict the temporal evolution of jet penetration and cone angle, transient simulations (limited to Case A only) are performed. Injection pressure oscillations are neglected during the overall injection event and, as stated earlier, the measured needle lift is accounted for morphing the computational grid. The simulated time is 0.9 ms to reach fully developed jet conditions, while limiting the CPU requirements. To monitor the temporal evolution of the jet, a mass fraction based iso-surface of the injected gas at 0.02 is considered following the sensitivities reported in literature [45], showing such threshold as a suitable maximum density gradient indicator when injecting H_2. However, considering the uncertainties related to the adoption of different gases and test conditions, which may slightly affect the selection of the mass fraction threshold, reasonable error bandwidths are included when comparing CFD and experimental results considering higher (0.05) and lower (0.001) values with respect to the selected one.

A comparison between Exp and CFD penetration is reported in Fig. 17 (A, B and C) for all the tested gases; similarly to the steady-state analyses, results with H_2 are included as a benchmark. The measured similarities comparing Ar and N_2 cases are well represented by the CFD model, as well as the jet penetration increase when injecting He. The alignment between experiments and simulations is reasonable with a maximum relative error of -15 % in the Ar and N_2 cases (in between 400 and 500 μs), while a 8 % overestimation of jet penetration is found in the He case at 1000 μs considering the 0.02 mass fraction threshold. The sensitivity of the penetration results on the mass fraction threshold is not negligible and it increases moving from high to low density gases. The delta comparing the three considered thresholds is between ±2 % for Ar and N_2 while increases to ±3 % with He and it is maximum and equal to ± 4 % with H_2; such behaviour is expected due to the higher mass diffusivity of H_2 compared to the other gases. The average absolute error is anyhow acceptable, comparable in all cases and lower than 10 %: Ar 6.2 %, N_2 6.4 % and He 6.4 %.

Penetration during the static injection phase (after 600 μs) is similarly underpredicted with higher density gases while it is slightly overestimated with He. A consistent trend as in the experiments is found replacing the injected gas, i.e. a non-negligible increase in jet penetration comparing He and H_2 to Ar and N_2. The penetration of the H_2 jet evolves similarly to He one, which is confirmed to be the inert gas better reproducing the overall H_2 behaviour; in particular, a higher penetration length (+3%) should be expected replacing He with H_2. Comparing Ar and N_2 with H_2, as reported in Fig. 17(D) the delta is relevantly higher. Focusing on the static injection phase, an increase of the penetration between 25 % and 30 % should be expected when replacing the two denser gases with H_2.

A comparison between CFD and experiments in terms of jet morphology at three different timings, during the static injection phase, is reported in Appendix B. CFD jet iso-lines are superimposed to the

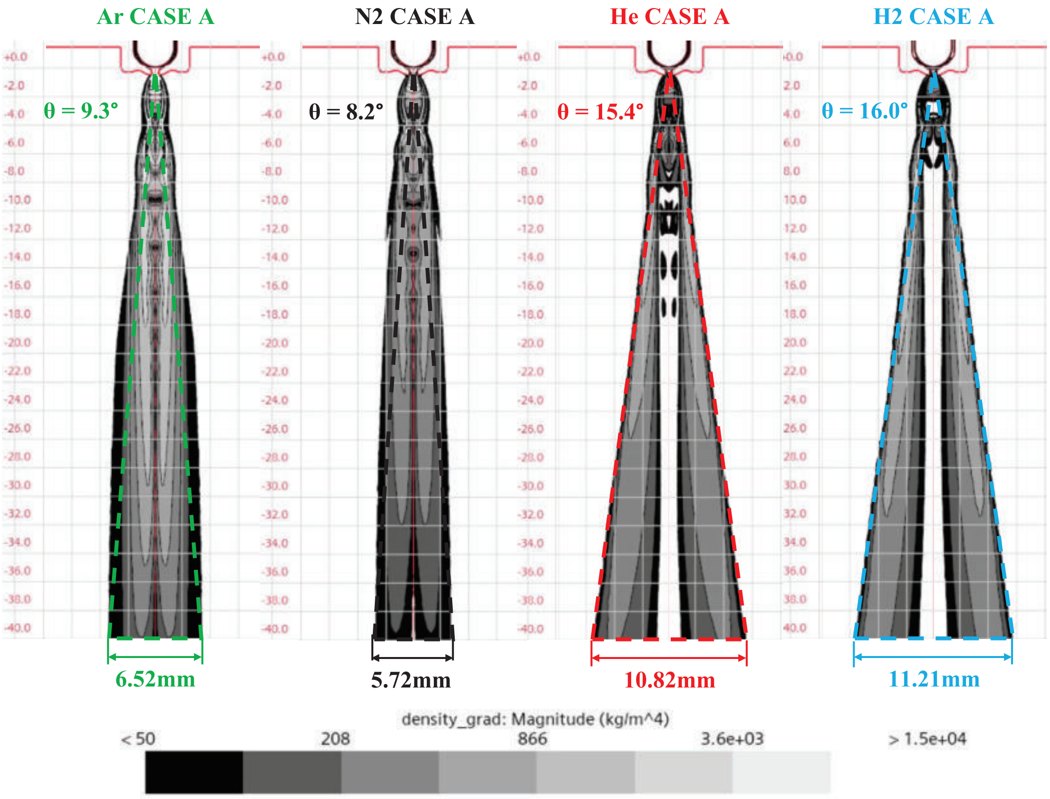

Fig. 16. Steady-state cone angle evaluation considering CFD density gradient scalar field.

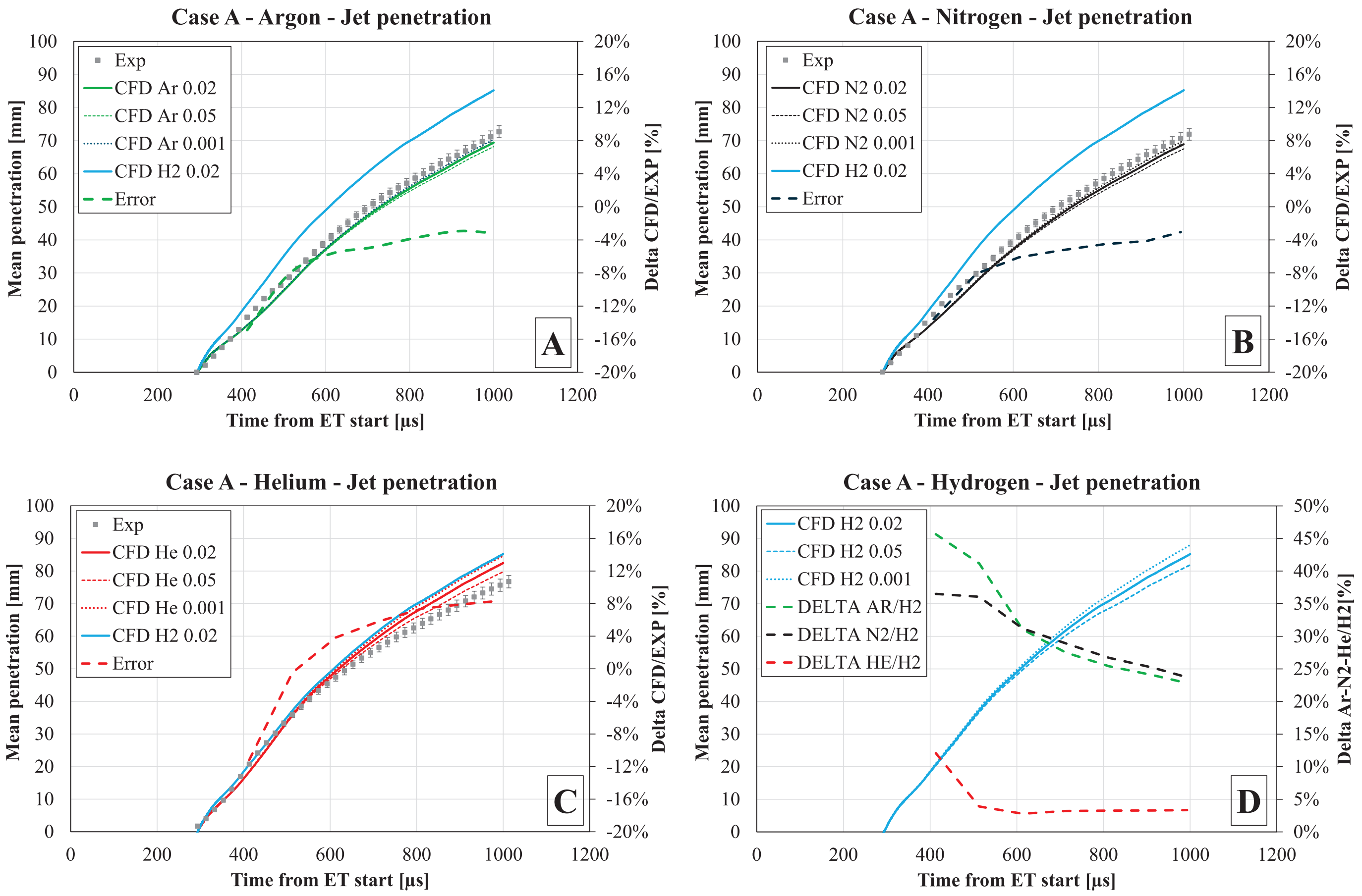

Fig. 17. EX/CFD comparison of gas jet penetration considering 0.05, 0.02 and 0.001 mass fraction thresholds for Ar (A), N_2 (B) and He (C) in Case A operation. In A, B and C the relative error comparing CFD (0.02 threshold) and experiments is reported. In D the percentage delta in terms of jet penetration comparing H_2 with other gases is reported.

experimental images and a sensitivity to the threshold value adopted to identify the jet is reported. As for penetration, three different mass fraction thresholds of 0.001, 0.02 (the reference one) and 0.05 are considered; similarly, 5, 10 and 15 kg/m^4 are selected as thresholds for density gradient based jet tracking. When the jet contour is identified, as from to the Schlieren images, penetration length and cone angle can be estimated. Focusing on the last, the maximum radial width and the axial position of the same point, for each timing, can be extracted from the simulations to calculate the cone angle trough trigonometry.

Analysing the mass fraction results (Appendix B), a higher jet penetration sensitivity to the selected threshold for He is visible, confirming the observations from Fig. 17. Changing the reference value, the

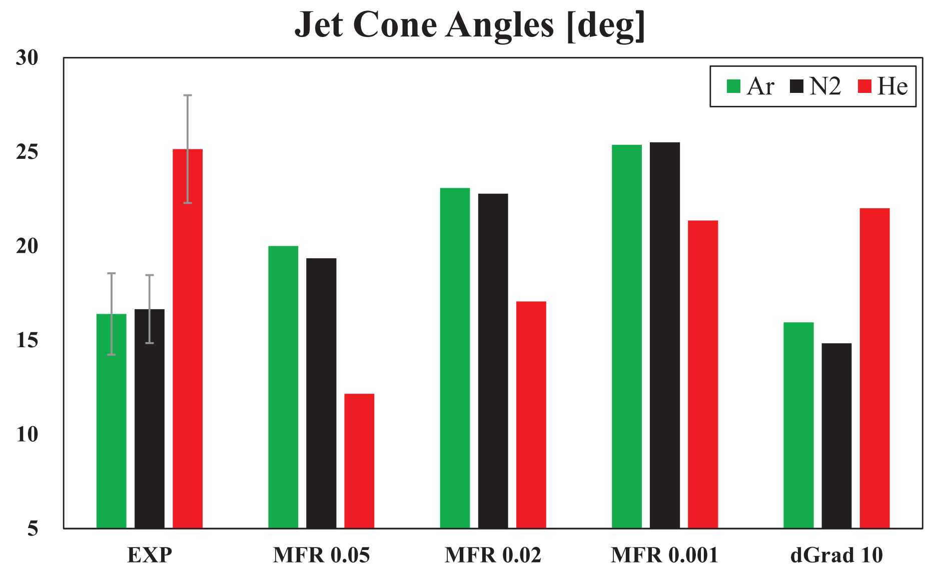

Fig. 18. Impact of the selected threshold on the cone angle estimation in CFD simulations.

absolute estimated jet penetration changes, but the relative trend comparing the gases is independent of the selected mass fraction threshold, confirming the reliability of the adopted approach in estimating the jet penetration length. Still focusing on mass fraction-based iso-lines, very similar drop-shaped jet morphologies are noticed for all the gases, and a high sensitivity of the estimated cone angle to the threshold value is expected.

An overall picture of the calculated cone angles from CFD is reported in Fig. 18. The calculation is performed at 633, 793 and 933 μs and the average value is reported in the graph; the error bandwidths are based on average measured standard deviation in the same time window. As for the penetration, an increase of the cone angle reducing the mass fraction threshold is detected. At first sight, the inability of the model in reproducing the cone angle variation changing the injected gas is quite evident. In particular, the cone angle is overestimated in Ar and N_2 cases due to overestimated jet width far from the nozzle tip, while it is matched in He cases when using the lowest mass fraction threshold. Generally speaking, differences in the jet morphology from the Schlieren images are poorly seen in the simulations when adopting a mass fraction-based jet tracking method.

To further deepen the Exp/CFD comparison, the same analysis is repeated by using a density gradient-based jet tracking method. Also in this case, 3 different thresholds are compared and superimposed to the experimental images as reported in Appendix B. Comparing the two methods, an opposite trend is found in terms of sensitivity to the adopted threshold. It is very low in He case (almost superimposed lines) thanks to the highest difference between the background and the injected gas density, which helps in sharply tracking the jet as in the experiments. With Ar, increasing the density gradient threshold up to 15 kg/m^4 the jet shape changes becoming closer to the experimental one. The cone angle reduces while the penetration is comparable to the one detected using the 0.02 mass fraction threshold. As for N_2, a different and narrower jet shape is tracked when using density gradient instead of mass fraction leading to a lower calculated cone angle. The jet width the cone angle are marginally affected by changes in the threshold value which, conversely, relevantly affects the penetration length.

Wrapping up the sensitivity analysis, it is possible to conclude that a density gradient-based method can better reproduce the evolution of the jet shape and cone angle varying the injected gases, as reported in Fig. 18. The identification of a proper threshold is therefore needed and it may change varying not only the injected gas characteristics but also the pressure ratio. In the presented analysis, a density gradient value of 10 kg/m^4 appear as the best compromise to well infer the jet cone angle with a penetration length consistent to the experimental target. It is important to stress that the impact of the density gradient threshold selection decreases when approaching lower density gases such as He or H_2 (Appendix B). In the case of He injection, moving the density gradient threshold between 5 and 15 kg/m^4 leads to very similar outcomes (see Fig. B3).

A comparison of the simulated jet shape evolution for the 4 considered gases can be found in Fig. 19, using the previously identified density gradient value of 10 kg/m^4. The highest penetration as well as cone angle of He compared to Ar and N_2 is further confirmed by the transient simulations. H_2 behaves very similarly to He: a slightly higher penetration and similar cone angle is expected. Close attention must be paid when replacing H_2 with heavier inert gases resulting in lower penetrations and cone angles despite the similarities in the near nozzle Mach disk shape.

As a final comparison, the same post-processing as in the experiments (see Fig. 10) is proposed in Fig. 20 for the CFD results, reporting the calculated jet penetration (A) and cone angle (B). The percentage delta with respect to the He case is also reported. Comparing the jet

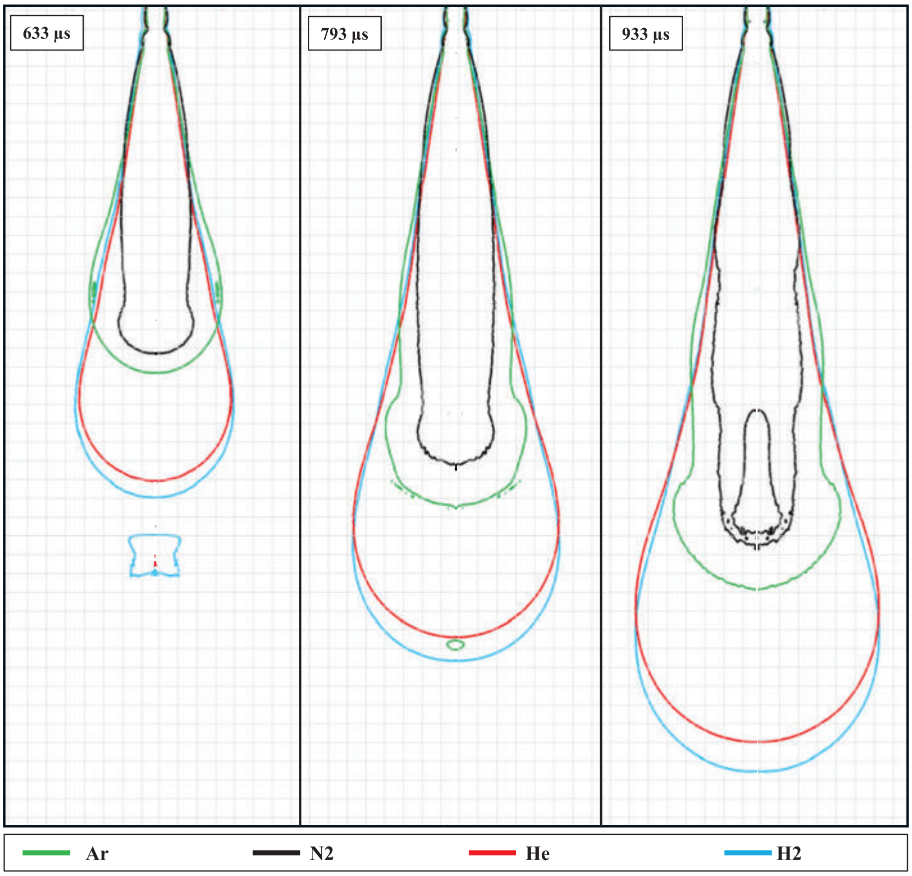

Fig. 19. Numerical temporal evolution of the gas jet with all the tested simulated gases considering density gradient iso-line value equal to 10 kg/m^4.

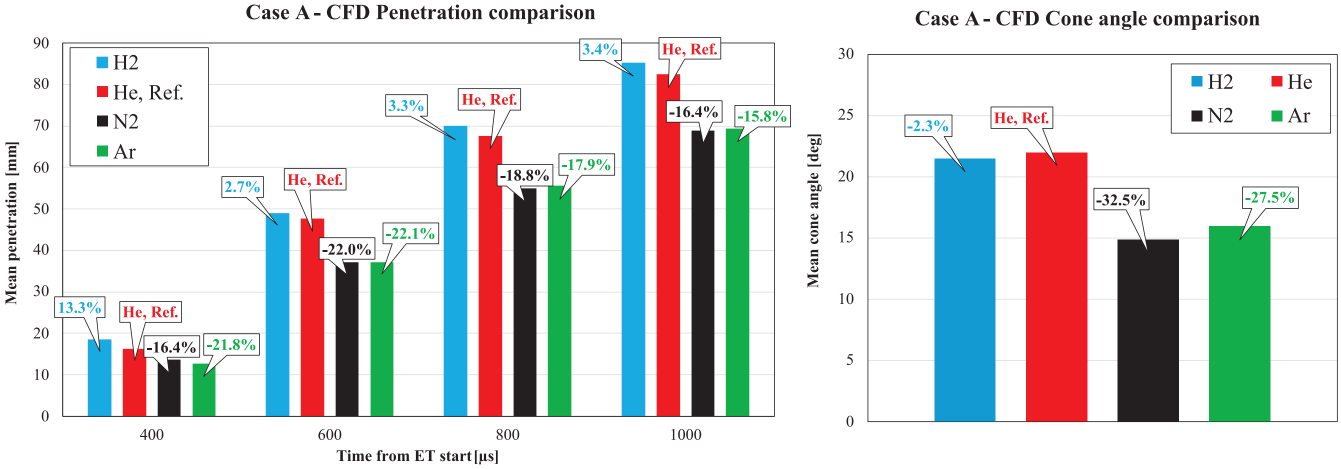

Fig. 20. Summary of CFD penetration lengths and cone angle changing the injected gases.

penetration length, the relative trend between the different gases is well represented by the model, notwithstanding the increased delta comparing He with Ar and N_2 due to overprediction of the penetration for the former and underestimation for the latter. As for the cone angle, a very similar trend between experiments and CFD is detected when using a density gradient based threshold instead of a mass fraction based one. A very similar behavior is found comparing He and H_2.

5. Conclusions

In the present work an experimental and numerical analysis on the behaviour of a prototype gas jet injector is discussed. A single plume jet is produced by a single-hole low-pressure direct injector derived by a GDI unit, using three different types of inert gas: Ar, N_2, and He.

The jet evolution is experimentally characterized in terms of mean flowrate (linearity curves) with the three gases, evidencing significant effects of the molecule structure on the flow. The analysis confirms the possibility of scaling the results of one gas to estimate the flow curve of a second gas via the ratio of the theoretical flow rates under chocked conditions. This result corroborates the significance of obtaining preliminary flow characteristics for a given injection system to be fed with H_2 by using safer inert gases, at least for the early-stage development phase of the injection system.

Further, the jet overall evolution is analysed by Schlieren imaging obtaining the jet tip penetration and cone angle time-histories for 2 and 4 MPa injection pressure versus atmospheric conditions for the examined inert gases. The results evidence significant differences in both jet penetration and cone angle, with a significantly smaller penetration rate for N_2 and Ar compared to He (ranging between −5% and −7%). At the same time, N_2 and Ar evidence a considerably smaller jet cone angle then He (33 % to 36 % narrower jet cone). Globally, the jet development analysis shows how the use of surrogate gases can easily lead to incorrect results in terms of plume evolution analysis.

The injector needle is simultaneously measured during the injector wet operation, globally providing appropriate boundary conditions for the 3D-CFD simulation of the injection process. After a validation of the numerical setup using the available experimental data pertaining to inert gases, a numerical extrapolation to H_2 injection is performed for both steady and unsteady simulations.

The models are validated on the available experimental measurements confirming the reliability of the proposed CFD methodology, which complements the experimental tests to derive the following main outcomes:

- The CFD model well performs in reproducing the flow rate variation changing injected gas and injection pressure. The simulations confirm the low variation in the discharge coefficient in all the tested conditions also when injecting Hydrogen.
- The Mach disk shape and the under-expansion near nozzle region shows the influence of the atomic structure of the gases. Similarities are therefore found between Ar and He, and between N_2 and H_2 respectively. The same trend is found comparing the main characteristic lengths, with a higher Mach disk width detected for N_2 and H_2.
- A weak correlation between Jet cone angle and Mach disk shape is found. Despite the similarities in the near nozzle region between N_2 and H_2, a higher cone angle, similar to the that of He, is detected injecting H_2, suggesting that the overall jet development is largely determined by diffusion mechanisms well downstream the Mach disk region.
- The definition of a correct and reliable threshold to track the gas jet evolution in CFD may be not trivial. A mass fraction-based threshold can well reproduce the jet penetration evolution while some misleading conclusions on jet morphology (and cone angle) are detected. Density gradient based method is proposed to better track the gas jet morphology, cone angle and penetration. In the simulated conditions, the experimental cone angle is matched well using a 10 kg/m^4 density gradient magnitude.
- Comparing the spatial and temporal evolution of the global jet, a similar morphology is found for He and H_2 confirming the suitability of He as an inert gas for the characterization of a H_2 injector.

The combined experimental and numerical study allows for definitive conclusions regarding the substitution of H_2 with inert gases. Strong similarities between He and H_2 confirm He as the best surrogate gas candidate to characterize jet cone angle and penetration. Slightly higher penetration (<5%) and similar cone angles are expected with H_2. If a detailed investigation of the near nozzle region and the Mach disk structure and characteristic lengths is targeted, the replacement of H_2 with a bi-atomic gas such as $N_2$is preferable, as nearly identical results are expected.

In future research, the objective will be a more comprehensive validation of the observed trends using different injector configurations including pintle and pintle-with-cap designs. Of particular interest could be the application of diagnostics such as the momentum flux distribution analysis to investigate the inner gas-jet structure in case of complex nozzle designs, again complemented by numerical analyses.

The final goal is to achieve a thorough understanding of H_2 injection and jet-air mixing processes, so to support the design of the combustion chamber and, in general, of all components involved in the operation of high-pressure gas jets.

CRediT authorship contribution statement

Sebastiano Breda: Writing – original draft, Visualization, Validation, Supervision, Software, Methodology, Investigation, Formal analysis, Data curation, Conceptualization. **Mauro Magnani:** Writing – original draft, Visualization, Validation, Software, Methodology, Investigation, Formal analysis, Data curation, Conceptualization. **Manuel Martino:** Writing – original draft, Visualization, Validation, Software, Methodology, Investigation, Formal analysis, Data curation, Conceptualization. **Stefano Fontanesi:** Writing – review & editing, Validation, Supervision, Resources, Project administration, Funding acquisition, Conceptualization. **Lucio Postrioti:** Writing – review & editing, Writing – original draft, Validation, Supervision, Resources, Project administration, Methodology, Funding acquisition, Formal analysis, Conceptualization.

Declaration of competing interest

The authors declare the following financial interests/personal relationships which may be considered as potential competing interests: Stefano Fontanesi reports financial support was provided by European Union, NextGenerationEU - National Sustainable Mobility Center - MOST, CN00000023, Italian Ministry of University and Research, Spoke 12 (CUP E93C22001070001). Sebastiano Breda reports financial support provided by the Department of Engineering “Enzo Ferrari” (University of Modena e Reggio Emilia), under the “FAR Dipartimentale 2023-24” project. If there are other authors, they declare that they have no known competing financial interests or personal relationships that could have appeared to influence the work reported in this paper..

Acknowledgments

Marelli Europe is warmly acknowledged for the support in providing the prototype gas injector used in the present research activity. Sebastiano Breda and Stefano Fontanesi acknowledge the financial support provided by the Department of Engineering “Enzo Ferrari” (University of Modena e Reggio Emilia), under the “FAR Dipartimentale 2023-24” project and the financial support provided by “European Union-Next generation EU trough the “PIANO NAZIONALE DI RIPRESA E RESILIENZA (PNRR) – MISSION 4 COMPONENTE 2, “Dalla ricerca all’impresa” INVESTIMENTO 1.4, (CN00000023). In the context of the “Sustainable Mobility Center (Centro Nazionale per la Mobilità Sostenibile – CNMS)” - Spoke 12 - Avviso MUR 3138/2021 modificato con DD 3175/2021”.

Appendix A

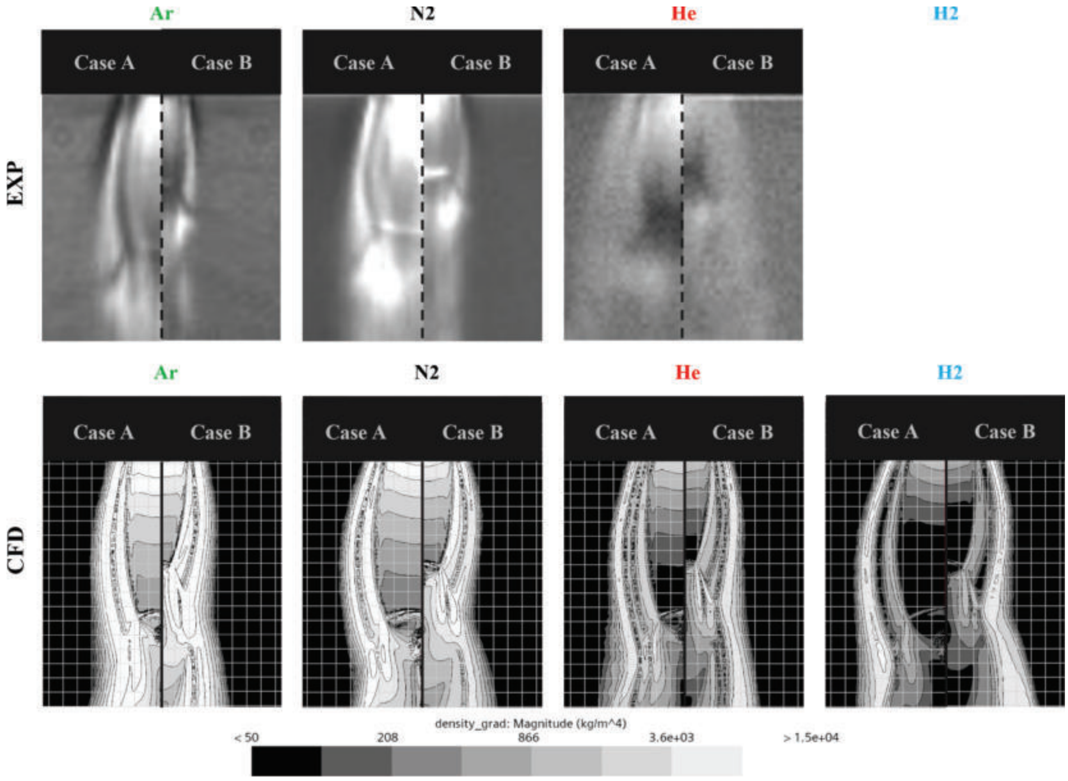

Fig. A1. Mach cone bell-shaped region Schlieren images (upper) for Case A (left) and Case B (right) with all the tested gases. Density gradient magnitude CFD scalar field (down) for Case A (left) and Case B (right) with all the simulated gases.

Appendix B

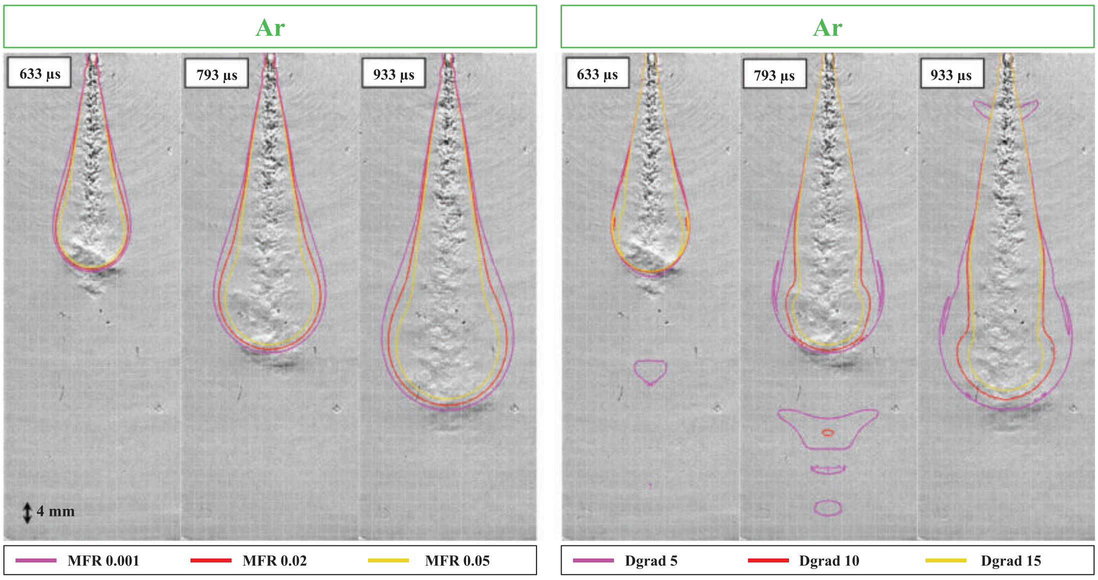

Fig. B1. Exp/CFD comparison of Ar gas Jet Morphology. Mass fraction based iso-lines of CFD results (left) compared to Density gradient iso-lines (right) superimposed to Schlieren experimental acquisition at 633, 793 and 933 µs.

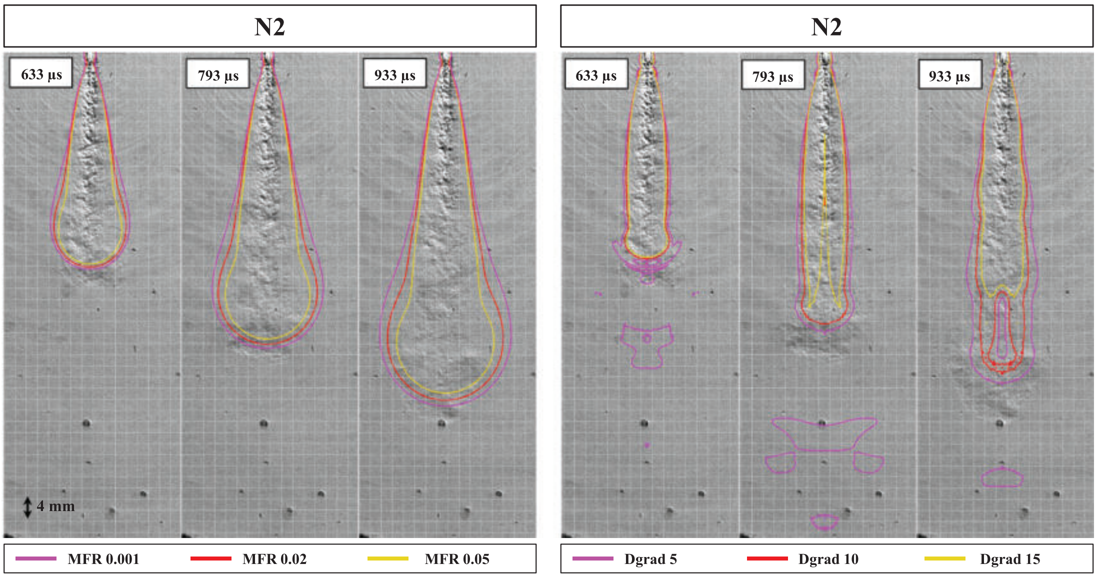

Fig. B2. Exp/CFD comparison of N_2 gas Jet Morphology. Mass fraction based iso-lines of CFD results (left) compared to Density gradient iso-lines (right) superimposed to Schlieren experimental acquisition at 633, 793 and 933 µs.

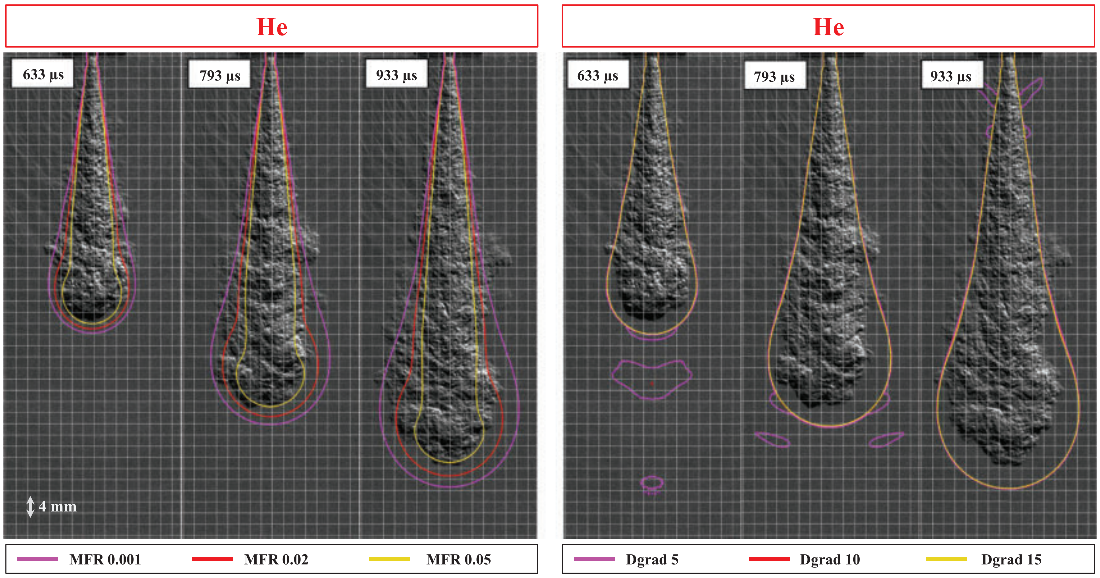

Fig. B3. Exp/CFD comparison of He gas Jet Morphology. Mass fraction based iso-lines of CFD results (left) compared to Density gradient iso-lines (right) superimposed to Schlieren experimental acquisition at 633, 793 and 933 µs.

Data availability

Data will be made available on request.

References

[1] Paris Agreement n.d. https://climate.ec.europa.eu/eu-action/international-action-climate-change/climate-negotiations/paris-agreement_en (accessed January 20, 2023).

[2] Regulation (EU) 2023/851 of the European Parliament and of the Council of 19 April 2023 amending Regulation (EU) 2019/631 as regards strengthening the CO_2 emission performance standards for new passenger cars and new light commercial vehicles in line with the Union's increased climate ambition (Text with EEA relevance). vol. 110. 2023.

[3] EU ban on sale of new petrol and diesel cars from 2035 explained | News | European Parliament 2022. https://www.europarl.europa.eu/news/en/headlines/economy/20221019STO44572/eu-ban-on-sale-of-new-petrol-and-diesel-cars-from-2035-explained (Accessed January 20, 2023).

[4] Fit for 55: zero CO_2 emissions for new cars and vans in 2035 | News | European Parliament 2023. https://www.europarl.europa.eu/news/en/press-room/20230210IPR74715/fit-for-55-zero-co2-emissions-for-new-cars-and-vans-in-2035 (Accessed 16 February 2023).

[5] Baade WF, Parekh UN, Hydrogen RVS. Kirk-Othmer Encyclopedia of Chemical Technology. John Wiley & Sons, Ltd; 2001.

[6] Kothari R, Buddhi D, Sawhney RL. Comparison of environmental and economic aspects of various Hydrogen production methods. Renew Sustain Energy Rev 2008; 12:553–63. https://doi.org/10.1016/j.rser.2006.07.012.

[7] Mohammadi A, Mehrpooya M. A comprehensive review on coupling different types of electrolyzer to renewable energy sources. Energy 2018;158:632–55. https://doi.org/10.1016/j.energy.2018.06.073.

[8] Kaiwen L, Bin Y, Tao Z. Economic analysis of Hydrogen production from steam reforming process: a literature review. Energy Sources Part B: Econ Plan Policy 2018;13:109–15. https://doi.org/10.1080/15567249.2017.1387619.

[9] Law CK. Combustion physics. Cambridge University Press; 2010.

[10] Züttel A. Hydrogen storage methods. Naturwissenschaften 2004;91:157–72. https://doi.org/10.1007/s00114-004-0516-x.

[11] Zheng J, Liu X, Xu P, Liu P, Zhao Y, Yang J. Development of high pressure gaseous Hydrogen storage technologies. Int J Hydrogen Energy 2012;37:1048–57. https://doi.org/10.1016/j.ijhydene.2011.02.125.

[12] Rivard E, Trudeau M, Zaghib K. Hydrogen storage for mobility: a review. Materials 2019;12:1973. https://doi.org/10.3390/ma12121973.

[13] Okonkwo PC, Barhoumi EM, Ben Belgacem I, Mansir IB, Aliyu M, Emori W, et al. A focused review of the Hydrogen storage tank embrittlement mechanism process. Int J Hydrogen Energy 2023. https://doi.org/10.1016/j.ijhydene.2022.12.252.

[14] Li H, Cao X, Liu Y, Shao Y, Nan Z, Teng L, et al. Safety of Hydrogen storage and transportation: an overview on mechanisms, techniques, and challenges. Energy Rep 2022;8:6258–69. https://doi.org/10.1016/j.egyr.2022.04.067.

[15] Yip HL, Srna A, Yuen ACY, Kook S, Taylor RA, Yeoh GH, et al. A review of hydrogen direct injection for internal combustion engines: towards carbon-free combustion. Appl Sci 2019;9:4842. https://doi.org/10.3390/app9224842.

[16] Cheng X, Baigang S, Zhen H. Investigation on jet characteristics of hydrogen injection and injection strategy for backfire control in a port fuel injection hydrogen engine. Energy Procedia 2017;105:1588–99. https://doi.org/10.1016/j.egypro.2017.03.508.

[17] Gao J, Wang X, Song P, Tian G, Ma C. Review of the backfire occurrences and control strategies for port Hydrogen injection internal combustion engines. Fuel 2022;307:121553. https://doi.org/10.1016/j.fuel.2021.121553.

[18] Li Y, Gao W, Zhang P, Fu Z, Cao X. Influence of the equivalence ratio on the knock and performance of a Hydrogen direct injection internal combustion engine under different compression ratios. Int J Hydrogen Energy 2021;46:11982–93. https://doi.org/10.1016/j.ijhydene.2021.01.031.

[19] Sfriso S, Berni F, Fontanesi S, d'Adamo A, Breda S, Teodosio L, et al. Combination of G-equation and detailed chemistry: an application to 3D-CFD hydrogen combustion simulations to predict NOx emissions in reciprocating internal combustion engines. Int J Hydrogen Energy 2024;89:161–76. https://doi.org/10.1016/j.ijhydene.2024.09.252.

[20] Franquet E, Perrier V, Gibout S, Bruel P. Free underexpanded jets in a quiescent medium: a review. Prog Aerosp Sci 2015;77:25–53. https://doi.org/10.1016/j.paerosci.2015.06.006.

[21] Belan M, De Ponte S, Tordella D. Highly underexpanded jets in the presence of a density jump between an ambient gas and a jet. PhysRevE 2010;82:026303. https://doi.org/10.1103/PhysRevE.82.026303.

[22] Raman G. Advances in understanding supersonic jet screech: review and perspective. Prog Aerosp Sci 1998;34:45–106. https://doi.org/10.1016/S0376-0421(98)00002-5.

[23] Ashkenas H, Sherman FS. In: deLeeuw JH, editor. Proceedings of the 4th International Symposium on Rarefied Gas Dynamics. Vol II, Academic, New York; 1966. p. 84.

[24] Crist S, Glass DR, Sherman PM. Study of the highly underexpanded sonic jet. AIAA J 1966;4:68–71. https://doi.org/10.2514/3.3386.

[25] Johansen LCR, de Sienes EDB, Dahlander P. Analysis of transient compressible gas jets using high speed Schlieren imaging. Warrendale, PA: SAE International; 2013.

[26] Konagaya R, Naitoh K, Tsuru K, Takagi Y, Mihara Y. Unsteady three-dimensional computations of the penetration length and mixing process of various single high-speed gas jets for engines. Warrendale, PA: SAE International; 2017.

[27] Yu J, Vuorinen V, Kaario O, Sarjovaara T, Larmi M. Visualization and analysis of the characteristics of transitional underexpanded jets. Int J Heat Fluid Flow 2013; 44:140–54. https://doi.org/10.1016/j.ijheatfluidflow.2013.05.015.

[28] Zhao J, Liu W, Liu Y. Experimental investigation on the microscopic characteristics of underexpanded transient Hydrogen jets. Int J Hydrogen Energy 2020;45: 16865–73. https://doi.org/10.1016/j.ijhydene.2020.04.140.

[29] Lee S, Kim G, Bae C. Behavior of Hydrogen hollow-cone spray depending on the ambient pressure. Int J Hydrogen Energy 2021;46:4538–54. https://doi.org/10.1016/j.ijhydene.2020.11.001.

[30] Hajialimohammadi A, Edgington-Mitchell D, Honnery D, Montazerin N, Abdullah A, Agha MM. Ultra high speed investigation of gaseous jet injected by a single-hole injector and proposing of an analytical method for pressure loss prediction during transient injection. Fuel 2016;184:100–9. https://doi.org/10.1016/j.fuel.2016.06.112.

[31] White TR, Milton BE. Shock wave calibration of under-expanded natural gas fuel jets. Shock Waves 2008;18:353–64. https://doi.org/10.1007/s00193-008-0158-6.

[32] Li M, Wu H, Liu X, Wei Z, Tian H, Zhang Q, et al. Numerical investigations on pilot ignited high pressure direct injection natural gas engines: a review. Renew Sustain Energy Rev 2021;150:111390. https://doi.org/10.1016/j.rser.2021.111390.

[33] Anaclerio G, Capurso T, Torresi M, Camporeale SM. Numerical characterization of Hydrogen under-expanded jets with a focus on Internal Combustion Engines applications. Int J Engine Res 2023:146808742211487. https://doi.org/10.1177/14680874221148789.

[34] Ruggles AJ, Ekoto IW. Ignitability and mixing of underexpanded Hydrogen jets. Int J Hydrogen Energy 2012;37:17549–60. https://doi.org/10.1016/j.ijhydene.2012.03.063.

[35] Hamzehloo A, Aleiferis PG. Gas dynamics and flow characteristics of highly turbulent under-expanded Hydrogen and methane jets under various nozzle pressure ratios and ambient pressures. Int J Hydrogen Energy 2016;41:6544–66. https://doi.org/10.1016/j.ijhydene.2016.02.017.

[36] Li X, Wu K, Yao W, Fan X. A comparative study of highly underexpanded Nitrogen and Hydrogen jets using large eddy simulation. Int J Hydrogen Energy 2016;41:5151–61. https://doi.org/10.1016/j.ijhydene.2016.01.120.

[37] Fontanesi S, Postrioti L, Magnani M, Martino M, Brizi G, Cicalese G. Preliminary Assessment of Hydrogen Direct Injection Potentials and Challenges through a Joint Experimental and Numerical Characterization of High-Pressure Gas Jets, 2022, p. 2022-24–0014. https://doi.org/10.4271/2022-24-0014.

[38] Settles GS. Schlieren and Shadowgraph techniques: visualizing phenomena in transparent media. Springer Science & Business Media; 2001.

[39] Postrioti L, Battistoni M, Ungaro C, Mariani A. Analysis of diesel spray momentum flux spatial distribution. SAE Int J Engines 2011;4:720–36.

[40] Cavicchi A, Postrioti L. Simultaneous needle lift and injection rate measurement for GDI fuel injectors by laser Doppler vibrometry and Zeuch method. Fuel 2021;285:119021. https://doi.org/10.1016/j.fuel.2020.119021.

[41] Postrioti L, Martino M, Fontanesi S, Breda S, Magnani M. Experimental and numerical momentum flux analysis of jets from a hydrogen injector. Warrendale, PA: SAE International; 2024.

[42] Cavicchi A, Postrioti L, Sorbini G, Brizi G. Local momentum flux measurement: an effective way for GDI spray targeting in flash boiling conditions. Fuel 2022;317:123454. https://doi.org/10.1016/j.fuel.2022.123454.

[43] Jassim FA. Semi-optimal edge detector based on simple standard deviation with adjusted thresholding. IJCA 2013;68:43–8. https://doi.org/10.5120/11555-6834.

[44] Soave G. Equilibrium constants from a modified Redlich-Kwong equation of state. Chem Eng Sci 1972;27:1197–203. https://doi.org/10.1016/0009-2509(72)80096-4.

[45] Kaczmarczyk KO, Liu X, Im HG, Turner JWG, Yuan H, Akehurst S, et al. Investigation of URANS CFD methods for supersonic hydrogen jets. SAE Technical Paper 2024. https://doi.org/10.4271/2024-01-2687.